Electronic and Optical Properties of Two-Dimensional $BaSi_2$

A Computational Investigation with van der Waals Density Functional Theory

Mohamed Ismail

Thesis submitted for the degree of
Master in Computational Science: Material Science
60 credits

Department of Physics
Faculty of mathematics and natural sciences

UNIVERSITY OF OSLO

Spring 2021

True knowledge exists
in knowing that you know nothing.

—Socrates

Electronic and Optical Properties of Two-Dimensional $BaSi_2$

http://www.duo.uio.no/

Printed: Reprosentralen, University of Oslo

Abstract

This work explores the possibilities of $BaSi_2$ as a two-dimensional structure utilizing density functional theory. To fully describe the properties of the two-dimensional structure, the bulk structure of $BaSi_2$ and $BaGe_2$ was studied first, where different approximations to the exchange correlation functional was used. From the results of the structural properties of the bulk structures, it was decided that the rev-vdW-DF2 functional was to be used for the further study of the bulk structures and the functional of choice regarding the investigation of the two-dimensional structure of $BaSi_2$. The results of the two-dimensional structure of $BaSi_2$ showed that the single layer of the 2D-layered system was unstable due to reconstruction. Thereafter, 2D-structures of $BaSi_2$ that consisted of multiple layers were explored, where the results showed no indication of reconstruction for such systems. Moreover, the results for the multilayered 2D systems showed that as the number of layers increased in the 2D-structure, it's properties became more and more similar to the properties of the bulk. $BaSi_2$ also possess a fundamental band gap energy that can be tuned from 1.41 eV (L3) to 1.30 eV (L5). The optical results of the 2D layered systems showed a weak anisotropic behaviour of the dielectric function and absorption coefficient. The 2D layered structures also seemed to have a broad range of absorption and a large absorption coefficient, where the highest absorption was calculated to be around $\sim 10^6$ cm^{-1}. These results makes the two dimensional structures of $BaSi_2$ an interesting candidate for applications in thin film applications, and recommended for experimental exploration.

Acknowledgements

I would like to take this opportunity to thank all the people that have helped me through this long and difficult journey known as a master thesis. First of all, I would like thank all my supervisors, Clas Persson, Konstantina Iordanidou and Lasse Vines. I would also like to express my utmost gratitude to my day-to-day supervisors, who have been essential for the realization of this thesis: Clas Persson for his invaluable advice and meticulous proof-reading of the thesis. Konstantina Iordanidou for her always being available to answer my silly questions and helping me with the setup of the DFT calculations. It is not an understatement to say that without them, there would be no thesis.
Secondly, I would like to thank the people that made the years as a student bearable and always interesting. Thank you Oliver, Bernhard, Jens and the rest of the people at MENA and CS for discussions, help on assignments, very long lunch breaks and listening to my never ending sessions of whining. At last I will like to thank my family and friends for patience and support throughout this process, even though they had no idea what I was working on.

Contents

Chapter 1

Introduction

Energy is essential for all life to exist and function properly. That is even more so true considering our modern society today, which is truly dependent on electricity, and as our global population increases by the minute, so will the energy demand of the world. According to the International Energy Agency (IEA), non-renewable energy resources was the highest contributing factor for generating electricity in the world in 2018 [1]. Continuing in this direction, where we mostly use non-renewable energy resources to generate electricity, will lead to higher emissions of greenhouse gases to the atmosphere, which in turn leads to increased global warming. Climate change is not something that is happening in the distant future, we are already experiencing some of the effects, such as more frequent extreme weather events like bush-fires, cyclones, droughts, floods, rising sea levels, more acidified oceans and increasing temperatures. In the future we will observe even more devastating effects of global warming, such as challenges in food production and supply of fresh water. The primary way to solve global warming is to eliminate the role of fossil fuels in modern society wherever possible. This means transitioning to renewable and carbon-free energy resources [2]. A renewable energy resource that has the possibility to solve all the energy problems we face today is the sun. In fact, the sun delivers more energy to Earth in one hour than humanity consumes over the course of a year [3].

Humanity's way of harnessing the energy of the sun is through the use of solar cells which converts sunlight into electricity. There exists many different types of solar cells, and one of them are thin-film solar cells, especially thin film solar cells made from cadmium telluride (CdTe) or copper indium gallium selenide (CIGS), have gained popularity. Unfortunately, these materials raises some issues, such as cost, supply and environmental, which adds on the difficulty level of developing solar cells for the future [4].

Therefore, the need for new materials are essential in the development of better solar cells. The search for new materials has led many to look towards two-dimensional (2D) materials, which refers to a material where one of the dimensions is nano-sized, and the shape of the material resembles a thin piece of paper. The reason why 2D materials have come into play are because they can lead to thinner, lighter and more flexible solar cells [5]. The popularity of 2D-materials have also risen, due to the fact that the dimensionality of a material have an effect on it's properties, similar to how the size of a material can affect it's properties. Graphene which was discovered in 2004, is a perfect example of where the dimensionality of a material had an affect on the materials behaviour, and it is often called the first 2D material. Since then, many other 2D materials have been discovered, such as transition metal dichalcogenides (TMDCs), where they have a layered structure with strong in-plane bonds and weak van der Waals (vdW) forces acting between the layers [6]. These materials have shown great potential to be used in solar cell applications, due to their excellent electron-transport properties and extremely high carrier mobility [5].

The search for new materials to be used in solar cell applications have not ceased, and many new candidates have been found in recent years. An example of such a candidate is $BaSi_2$, which contain abundant and inexpensive elements, and various experimental investigations have found the material $BaSi_2$ to possess promising material characteristics for thin-film technology. Nonetheless, to the author's best knowledge, there doesn't seem to have been any studies looking at the material as a possible 2D material, where we know from experience that materials tend to change their behaviour when the dimensions and sizes are varied.

Thus, the focus of this work will primarily be on the electronic structure and optical properties of 2D $BaSi_2$, and the potential use in thin film solar cells applications. First-principle calculations will be utilised to study these phenomenons, mainly density functional theory (DFT). Which is a computational quantum mechanical modelling method used in physics, chemistry and material science to investigate the electronic structure of many-body systems. This method uses a few different approximation, which will be discussed in the later chapters, to solve quantum mechanical systems far too complicated to be evaluated analytically. With this approach we are able to investigate properties of theoretically proposed or experimentally realised materials.

The thesis is structured as follows: First a brief review of material science, followed by some background information about the material $BaSi_2$. In Chapter 3, central theory of DFT is explained, to get an understanding of the computational methods used in this work. Chapter 4 deals with the practical aspects of DFT, such as the computational methods used as well as the approximations in those methods. Chapter 5 illustrates how the methods have been practically implemented. The numerical results are presented and discussed in Chapter 6. The work is concluded in Chapter 7, where it includes how the material can be investigated further.

Chapter 2

Background

2.1 Material Science

The scope of this section is to give a brief introduction to the fundamentals of material science. It is not intended to give a complete explanation of the theories, but merely give a short overview for the reader with no previous knowledge of material science.

2.1.1 Bonds

All materials are built up by an unimaginable number of atoms clustered together and they are held together by bonds between the atoms and/or molecules. There exists two types of bonds, interatomic and intermolecular bonds.

The interatomic bonds are bonds between atoms and involves the valence electrons of the atoms. There exists three types of interatomic bonds;

- **Ionic bonding**
  An ionic bond is formed when valence electrons are transferred from one atom to the other to complete the outer electron shell.
- **Covalent bonding**
  A covalent bond is formed when the valence electrons from one atom are shared between two or more particular atoms.
- **Metallic bonding**
  A metallic bond is formed when the valence electrons are not associated with a particular atom or ion, but exist as a "cloud" of electrons around the ion centers [7].

The intermolecular bonding is defined as bonding between one molecule and a neighbouring molecule. Intermolecular forces are much weaker than the interatomic forces, but they are important because they determine the physical properties of materials, like their boiling point, melting point, density, and enthalpies of fusion and vaporization. There also exists different types of intermolecular bondings, one such is van der Waals (vdW) forces, which is driven by induced electrical interactions between two or more atoms or molecules that are very close to each other [8].

2.1.2 Crystalline Structure

The atomic ordering of materials decides if the material is either crystalline or amorphous. If the material is crystalline it means that it has a long-range periodicity, and if it is amorphous it means having local ordering of the constituent atoms, but no long-range periodicity.

A crystal structure is composed of atoms, ions, or molecules arranged in a pattern that is repetitive in three-dimensions. The crystal is represented as a lattice, that is, a three-dimensional array of points (lattice points), each which has identical surroundings. The crystal lattice is defined by three translation vectors $\mathbf{a}_1$, $\mathbf{a}_2$ and $\mathbf{a}_3$, also called the lattice vectors. The displacements from one lattice point to another may be written as

$$\mathbf{R} = c_1\mathbf{a}_1 + c_2\mathbf{a}_2 + c_3\mathbf{a}_3 \tag{2.1}$$

where c_1, c_2, c_3 are integers. Also, the length of the lattice vectors are called the unit cell parameters, where a unit cell is defined as the smallest repeatable entity that can be used to completely represent the crystal structure. In other words, it is the building block of the crystal structure. Moreover, each crystal lattice is defined by a crystal system, and the collection of them are called Bravais lattices [7].

2.1.3 Reciprocal Space

All that we have discussed so far deals with structures in the real space. However, in material science, it is sometimes more advantageous to work in the reciprocal space, which is defined as the Fourier transform of the real space. The reciprocal space is also called the k-space or the momentum space. Just as we defined positions in real space in terms of the lattice vectors $\mathbf{a}_1$, $\mathbf{a}_2$ and $\mathbf{a}_3$, it is also possible to do the same thing in the reciprocal space. These vectors are called the reciprocal lattice vectors, $\mathbf{b}_1$, $\mathbf{b}_2$ and $\mathbf{b}_3$ and are defined as

$$\mathbf{b}_1 = 2\pi\frac{\mathbf{a}_2 \times \mathbf{a}_3}{\mathbf{a}_1 \cdot (\mathbf{a}_2 \times \mathbf{a}_3)}$$
$$\mathbf{b}_2 = 2\pi\frac{\mathbf{a}_1 \times \mathbf{a}_3}{\mathbf{a}_1 \cdot (\mathbf{a}_2 \times \mathbf{a}_3)}$$
$$\mathbf{b}_3 = 2\pi\frac{\mathbf{a}_1 \times \mathbf{a}_2}{\mathbf{a}_1 \cdot (\mathbf{a}_2 \times \mathbf{a}_3)}$$

Similar to the lattice vector in the real space, the displacement from one lattice point to another in reciprocal space can be defined as

$$\mathbf{G} = h\mathbf{b}_1 + k\mathbf{b}_2 + l\mathbf{b}_3 \tag{2.2}$$

where h, k, l are integers, and is referred as the vector coordinates (h, k, l) of the reciprocal space described by Miller indices. Furthermore, as we described a primitive cell in the real space, that can also be done in the reciprocal space and because that primitive cell has many special properties, it is given a name, it is called the Brillouin zone (BZ) [9].

2.1.4 Band Structure

According to quantum mechanics, particles have discrete energy levels, unlike in classical mechanics where the energy levels for particles are continuous. This means that particles in quantum systems can only have certain energy states, however, a crystalline material consists of many atoms, which contains many electrons, which means that the energy states interact and blend together. They form what is known as energy bands or band structure, which characterises the regions of energies allowed for electrons in the system [10]. Figure 2.1 illustrates energy bands forming for when many electrons come together.

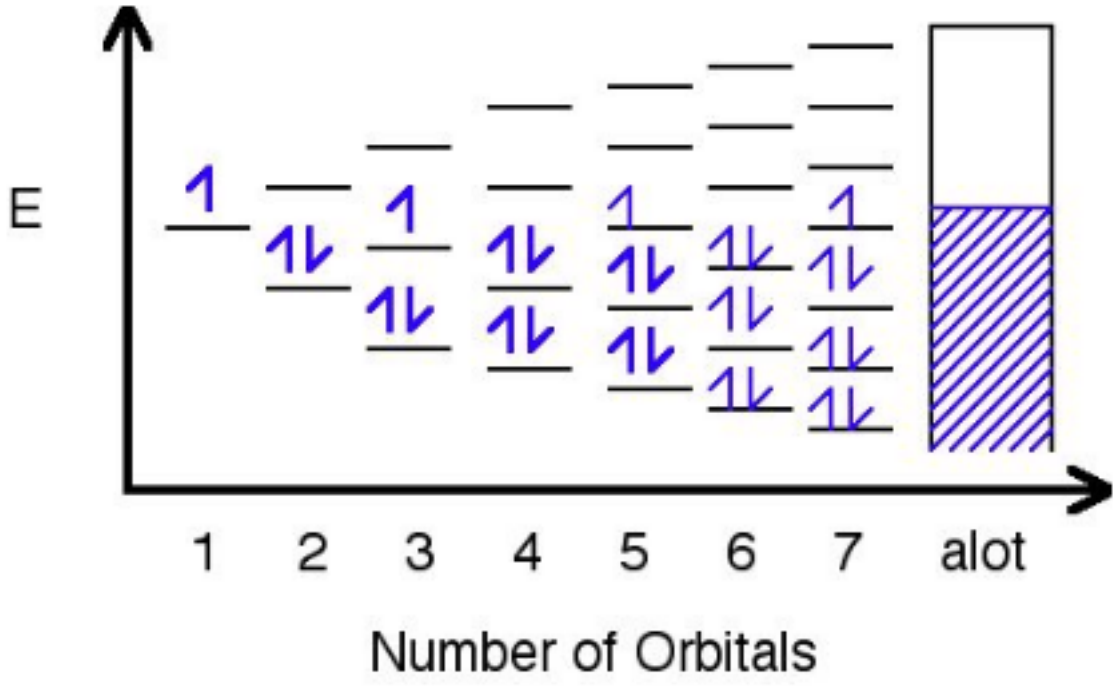

Figure 2.1: Orbitals are represented by the black horizontal lines, and they are being filled with an increasing number of electrons as their amount increases. Eventually, as more orbitals are added, the space in between them decreases to hardly anything, and as a result, a band is formed where the orbitals have been filled [10].

The band structure are determined by which atoms form the material, more exactly their orbitals. Therefore, the band structure can be different depending on the material, such as a metal, semiconductor and insulator. To explain the differences between them it is beneficial to introduce two terms that are important when discussing the band structure of materials. The terms are the conduction and valence band, known as the lowest unoccupied band and the highest occupied band, respectively [10]. Sometimes the valence band and the conduction band are separated by an energy difference denoted as E_g, and is called the band gap energy. Metals for example, have no band gap between their valence and conduction bands, since they overlap. Both the semiconductor and insulator on the other hand has a band gap, where the only difference between them is the size of the band gap.

Another distinct feature with the band structure of a material concerns whether the band gap, if it even has one, is direct or indirect.

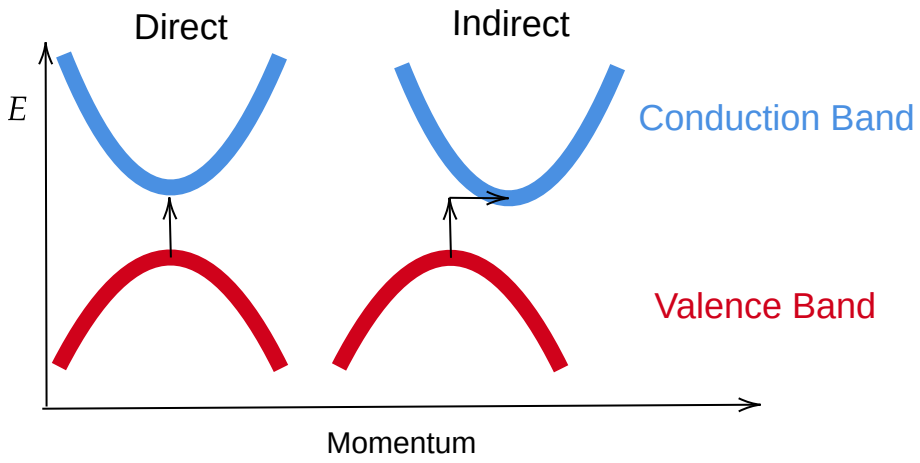

Figure 2.2: A schematic presentation of a direct and indirect band gap. The energy bands are plotted as lines in this plot of energy versus the momentum.

Figure 2.2 illustrates a direct and indirect band gap. A direct band gap means that the top of the valence band and the bottom of the conduction band of the material occur at the same **k**-point. Compared to an indirect band gap, where the maximum energy of the valence band occurs at a different **k**-point to the minimum in the conduction band energy. In the case for the direct band gap, the electrons only needs a change in energy to move from the valence band maximum (VBM) to the conduction band minimum (CBM), whereas for the indirect band gap, a change in both the energy and momentum is needed.

2.2 $BaSi_2$

Barium disilicide ($BaSi_2$) is a compound consisting of the group 2 element Barium (Ba) and the group 4 element Silicon (Si). In bulk, $BaSi_2$ has three possible structures, orthorhombic, cubic and trigonal. However, in this study we will be focusing on the orthorombic structure, which has the space group $D_{2h}^{16} - Pnma$ (no. 62). The unit cell of Barium silicide is shown below.

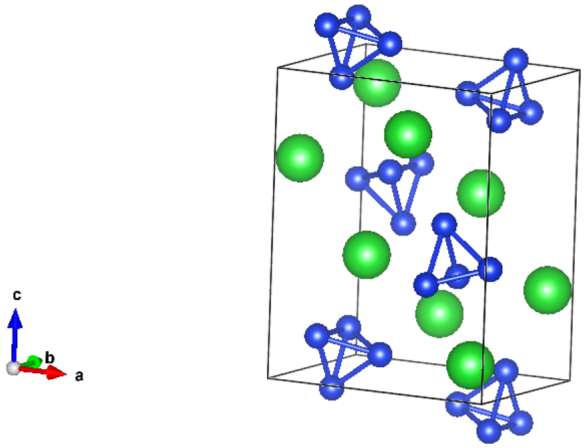

Figure 2.3: The atomic structure of $BaSi_2$. The green spheres represent barium atoms and the blue spheres represents the silicon atoms. This figure is produced using the software VESTA [11].

As illustrated above, one can observe that the silicon atoms are bonded together in a cluster of 4 atoms, where the binding in between those atoms are covalent, but the binding between the Ba-atoms and the Si-clusters are ionic.

The material $BaSi_2$ is not so unknown, the material have been gaining popularity lately, as it has showed interesting electronic and optical properties, which has led it to be studied for solar cell applications, both experimentally and computationally. For example, a previous DFT study using hybrid functional has shown that $BaSi_2$ possess an indirect bandgap of ~ 1.25 eV and a maximum absorption coefficient at 1.5×10^6 cm^{-1} [12]. Another example is an experimental study where it was reported a solar cell efficiency of approximately 10%, for a p-type $BaSi_2$/n-type Si with a film thickness of 40 nm [13]. One group that also studied the solar cells applications of $BaSi_2$ reported that a n- and p-type doping of $BaSi_2$ was possible, and that the hole concentration can be controlled in the wide range of $1016 - 1019$ cm^{-3} by Bor doping [14, 15].

Chapter 3

Theory

In the twentieth century, a physicist by the name of Erwin Schrödinger devised an equation that was able to describe systems that were at atomic levels, just as Newtons laws were able to describe systems at macroscopic levels. Thus, in order to analyze a material theoretically, one has to solve the quantum-mechanical Schrödinger equation for that material. Over the years, there have been devised numerous methods that aims to solve the Schrödinger equation, one such method is density functional theory and in this chapter, the basics of DFT will be described. To fully explain the theory behind DFT, some fundamental elements of quantum physics will also be described, such as the many-particle Schrödinger equation and the approximations surrounding it.

3.1 The Single-Electron Schrödinger Equation

In order to utilize the many-particle Schrödinger equation, it may be beneficiary to first study the single-electron case and build us up from there on.

The time-dependent Schrödinger equation for a single electron is written as [16]

$$i\hbar\frac{\partial}{\partial t}\Psi(\mathbf{r},t) = \hat{H}\Psi(\mathbf{r},t), \tag{3.1}$$

where $\Psi(\mathbf{r},t)$ is the electron wave function and $\hat{H}$ is the Hamiltonian, which contains the kinetic energy operator $\hat{T}$, and potential energy operator $\hat{U}$

$$\hat{H} = \hat{T} + \hat{U} = -\frac{\hbar^2\nabla^2}{2m_e} + V(\mathbf{r},t), \tag{3.2}$$

where m_e is the electron mass and $\hbar$ is planck's constant.

In the cases where the potential is independent of time, $V(\mathbf{r},t) = V(\mathbf{r})$, the Schrödinger equation can be solved by the method of separation of variables. That means the wavefunction can be expressed in the following manner:

$$\Psi(\mathbf{r},t) = \psi(\mathbf{r})\phi(t), \tag{3.3}$$

where $\psi(\mathbf{r})$ is purely a function of position and $\phi(t)$ is purely a function of time.

By plugging these expressions above, the Schrödinger equation now reads

$$i\hbar\psi(\mathbf{r})\frac{\partial\phi(t)}{\partial t} = \hat{H}\psi(\mathbf{r})\phi(t) \tag{3.4}$$

$$i\hbar\psi(\mathbf{r})\frac{\partial\phi(t)}{\partial t} = \Big(-\frac{\hbar^2\nabla^2}{2m_e} + V(\mathbf{r})\Big)\psi(\mathbf{r})\phi(t) \tag{3.5}$$

Dividing both sides of the equation by $\psi(\mathbf{r})\phi(t)$, we now get

$$i\hbar\frac{1}{\phi(t)}\frac{\partial\phi(t)}{\partial t} = -\frac{\hbar^2}{2m_e}\frac{1}{\psi(\mathbf{r})}\frac{\partial^2\psi(\mathbf{r})}{\partial x^2} + V(\mathbf{r}). \tag{3.6}$$

Now, the left hand side is a function of t alone, and the right hand side is a function of x alone. The only way this can possibly be true is if both sides are in fact constant, and it can be proven that the constant is equal to the total energy of the particle, which is denoted as E.

$$i\hbar\frac{1}{\phi(t)}\frac{\partial\phi(t)}{\partial t} = E \quad \rightarrow \quad \frac{\partial\phi(t)}{\partial t} = \frac{1}{i\hbar}E\phi(t)$$

$$-\frac{\hbar^2}{2m_e}\frac{1}{\psi(\mathbf{r})}\frac{\partial^2\psi(\mathbf{r})}{\partial x^2} + V(\mathbf{r}) = E \quad \rightarrow \quad -\frac{\hbar^2}{2m_e}\frac{\partial^2\psi(\mathbf{r})}{\partial x^2} + V(\mathbf{r})\psi(\mathbf{r}) = E\psi(\mathbf{r})$$

The equation dependent on time is a small matter to solve, the only thing needed to solve it is to multiply by ∂t and integrate the equation on both sides and the expression we are left with is

$$\phi(t) = e^{\frac{Et}{i\hbar}}. \tag{3.7}$$

The equation which is dependent on position is often referred to as the time-independent Schrödinger equation, and it is not solvable until the potential $V(\mathbf{r})$ is known. The rest of this chapter and thesis will focus on this equation, and every time we are referring to the Schrödinger equation, we mean the time-independent Schrödinger equation [16].

3.2 The Many-Particle Schrödinger Equation

Materials consist of electrons and nuclei, and to fully understand it's properties, the knowledge of it's electronic structure is needed. To describe a materials electronic structure, and determine their properties, one has to solve the many-particle Schrödinger equation for that system, which is defined as

$$H\Psi(\mathbf{r_1}, \mathbf{r_2}, \ldots, \mathbf{r_N}, \mathbf{R_1}, \mathbf{R_2}, \ldots, \mathbf{R_M}) = E\Psi(\mathbf{r_1}, \mathbf{r_2}, \ldots, \mathbf{r_N}, \mathbf{R_1}, \mathbf{R_2}, \ldots, \mathbf{R_M}) \tag{3.8}$$

where $\Psi(\mathbf{r_1}, \mathbf{r_2}, \ldots, \mathbf{r_N}, \mathbf{R_1}, \mathbf{R_2}, \ldots, \mathbf{R_M})$ is the total wavefunction of the material that contains all the information that can be known about the system, and where $\mathbf{r}_i$ describe the coordinates of the i-th electron and $\mathbf{R}_j$ describes the coordinates of the j-th nucleus [17]. Furthermore, E is the energy of the system described by Ψ and H is the Hamiltonian of the interacting system, which is illustrated in Figure 3.1.

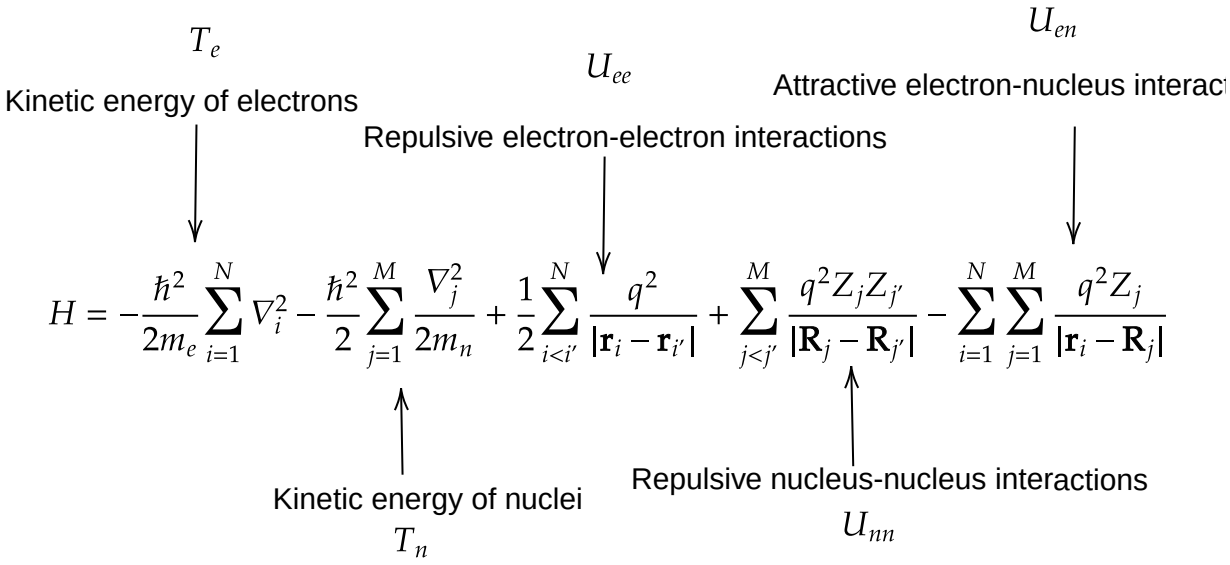

Figure 3.1: The terms of the many-particle Hamiltonian. The summation over $i < i'$ is to avoid double counting electron interactions, and to avoid self-interactions.

The analytical solution for the many-particle Schrödinger equation is limited to only simple systems, for example the hydrogen atom, because of the complicated expressions that describes the interactions between the electrons and nuclei. To make the equation more applicable, such that it is possible to study systems where there exists a large number of particles, approximations have to made.

3.3 The Born-Oppenheimer Approximation

One such an approximation was introduced in 1927, by Max Born and J. Robert Oppenheimer, which had the brilliant idea of separating the many-particle Schrödinger equation into an electron part and a nuclei part. Their reasoning was that since the nuclei is much heavier than the electrons, it was reasonable to assume that the nuclei could be treated as point charges. That is, if the nuclei moves, the electrons respond instantaneously. This argument made it possible to justify that one could do a variable separation on the many-particle Schrödinger equation, as shown below

$$\Psi(\mathbf{r}, \mathbf{R}) \approx \psi(\mathbf{r}, \mathbf{R})\phi(\mathbf{R}), \tag{3.9}$$

where $\Psi(\mathbf{r}, \mathbf{R})$ is the total wave function, and $\psi(\mathbf{r}, \mathbf{R})$ is the electronic wavefunction and has a dependency on the nuclei positions since when they move so does the electrons. Furthermore, $\phi(\mathbf{R})$ is the wave function of the nuclei.

By utilizing this approximation on the many-particle Schrödinger equation illustrated above in Equation 3.8, it can be shown that the equation can be separated into an electronic and a nuclear eigenvalue equation

$$\begin{aligned} [T_e + U_{ee} + U_{en}]\psi(\mathbf{r}, \mathbf{R}) &= E_e(\mathbf{R})\psi(\mathbf{r}, \mathbf{R}) \qquad \text{Electronic Schrödinger equation} \\ [T_n + U_{nn} + E_e(\mathbf{R})]\phi(\mathbf{R}) &= E_{tot}(\mathbf{R})\Theta(\mathbf{R}) \qquad \text{Nuclear Schrödinger equation.} \end{aligned}$$

These two equations are coupled via the electronic energy eigenvalue $E_e(\mathbf{R})$, which also depends on the nucleus positions through the wavefunction. Moreover, the kinetic energy of the nuclei, T_n

is often set to zero, since the nuclei is thought of as point charges. This means that the remaining terms one the left side of the nuclear Schrödinger equation is shortened down to $[U_{nn} + E_e(\mathbf{R})]$, and is denoted as the potential energy surface (PES), $E_p(\mathbf{R})$ [17].

3.4 The Hartree & Hartree-Fock Approximations

Another approximation was introduced in 1948, by a physicist named Hartree, which had an idea of how to express the many-electron wavefunction. The Hartree approximation starts by invoking an initial ansatz that the multi-electron wave function

$$\Psi(\mathbf{r}_1, \mathbf{r}_2, \ldots, \mathbf{r}_N) \tag{3.10}$$

can be expanded as a product of single-electron wave functions

$$\Psi(\mathbf{r}_1, \mathbf{r}_2, \ldots, \mathbf{r}_N) \approx \psi_1(\mathbf{r}_1)\psi_2(\mathbf{r}_2)\ldots\psi_N(\mathbf{r}_N), \tag{3.11}$$

which assumes that all the electrons are independent of each other, and that they only interact via the Coulomb potential. That means that the all the electrons can be described of the single-electron wavefunctions.

Such a many-electron wave function is termed a Hartree product, with electron-one being described by wavefunction ψ_1, electron-two being described by wavefunction ψ_2 and so on. The problem with this approximation is that the Hartree wavefunction is not anti-symmetric with respect to the particle coordinates. That is, the particles are distinguishable, and do not obey the Pauli exclusion principle for fermions. However, in 1950 a physicist named Fock modified the Hartree approximation to overcome this issue. This was done by constructing an anti-symmetric wavefunction which makes the electrons indistinguishable, which is illustrated below

$$\Psi(\mathbf{r}_1, \mathbf{r}_2, \ldots, \mathbf{r}_N) = \frac{1}{\sqrt{N!}} \begin{vmatrix} \psi_1(\mathbf{r}_1) & \psi_2(\mathbf{r}_1) & \ldots & \psi_N(\mathbf{r}_1) \\ \psi_1(\mathbf{r}_2) & \psi_2(\mathbf{r}_2) & \ldots & \psi_N(\mathbf{r}_2) \\ \vdots & \vdots & \ddots & \vdots \\ \psi_1(\mathbf{r}_N) & \psi_2(\mathbf{r}_N) & \ldots & \psi_N(\mathbf{r}_N) \end{vmatrix}. \tag{3.12}$$

The $\frac{1}{\sqrt{N!}}$ is there to normalize the wavefunction, and the determinant is called the Slater determinant. If the particles are interchanged here, the sign changes. In addition, if the electrons are in identical states, the wavefunction becomes zero. This approximation is denoted as a Hartee-Fock (HF) approximation, and since the HF method follows the Pauli exclusion principle, it is able to describe something called the exchange energy, which the Hartree method is not able to do. However, it is important to understand that neither the Hartree nor HF method are able to fully describe the many electron interaction problem. In the case of HF, it is not able to describe the correlation energy between the electrons [17].

3.5 The Variational Principle

In physics and chemistry one is mostly concerned with the ground state energy of the system one is studying. This can be accomplished by utilizing the variational principle, which states that for a given trial wave function Ψ_T, the expectation value of the Hamiltonian, $\hat{H}$ will be an upper bound to the ground state energy, E_0 of the system

$$E_0 \leq E = \frac{\int \Psi_T^* \hat{H} \Psi_T d\boldsymbol{r}}{\int \Psi_T^* \Psi_T d\boldsymbol{r}}. \tag{3.13}$$

In other words, to find the optimum trial wave function Ψ_T the total energy E is minimized by varying the trial wave function, and the wave function that minimizes the energy the most is the optimum trial wave function. Moreover, the variational principle tells us that only the

true ground state wave function will give the lowest total energy of the system, so the trial wave function that minimizes the energy the most will never get a energy lower than the true ground state wave function, but only slightly higher or equal to it.

In addition, the energy is often minimized with some constraints to make sure that the trial wave function not lose the desired functionalities, such as being normalized and/or that the functions that make up the trial wave function are orthogonal. This is accomplished by implementing the Langrange multiplier method [17].

3.6 Density Functional Theory

The density functional theory is a method which tries to solve the many-electron Schrödinger equation by reformulating the systems wave function, which is a function of $3N$ variables, in terms of the electron density $n(\mathbf{r})$, which is a function of three variables:

$$n(\mathbf{r}) = |\Psi(\mathbf{r}_1, \mathbf{r}_2, \ldots, \mathbf{r}_N)|^2, \tag{3.14}$$

where $\Psi(\mathbf{r}_1, \mathbf{r}_2, \ldots, \mathbf{r}_N)$ is the total wave function of the system.

The theory also states that all ground-state physical properties of the many-electron system are functionals of the ground-state electron density. Which means, that by knowing the ground-state density $n_0(\mathbf{r}) = |\Psi_0(\mathbf{r})|^2$, it should be possible to determine the total energy, magnetic moment, etc, of the system [17].

3.6.1 Hohenberg-Kohn Theorems

The basis for density functional theory stems from two fundamental mathematical theorems proved by P. Hohenberg and W. Kohn [18].

Theorem I:
For any system of interacting particles in an external potential $V_{ext}(\boldsymbol{r})$, the potential $V_{ext}(\boldsymbol{r})$ is determined uniquely (except for a constant) by the ground state density $n_0(\mathbf{r})$.

The first theorem presented above states that if one knows the electronic ground state density, one can determine the external potential uniquely. By knowing the external potential, the full Hamiltonian can be found, which in turn makes it possible to solve the Schrödinger equation to get the wave function, and this makes it possible to determine all the ground state properties of the system.

Theorem II:
A universal functional for the energy $E[n]$ can be defined in terms of the electron density. The exact ground state is the global minimum value of this functional.

The second theorem states that the ground state density $n_0(\mathbf{r})$ has the lowest energy, also known as the ground state energy E_0. The ground state density can be found by minimizing the energy as a functional of the density, $E[n]$, and this is accomplished by utilizing the variational principle explained earlier.

Proofs for both theorems can be found in Appendix A.1.

3.6.2 The Kohn-Sham Equation

The Hohenberg-Kohn theorems prove that there exists a unique functional $E[n(\boldsymbol{r})]$ for any electronic system, which is minimized for the unique ground-state density $n_0(\boldsymbol{r})$. However, there is no theorem on how to construct such a functional. A year after the Hohenberg-Kohn theorems

were published, a paper by Kohn and Sham [19] devised the Kohn-Sham equation which made DFT feasible.

The Kohn-Sham equation is based on the ansatz that the exact ground state density can be written as the ground state density of a fictitious system of noninteracting particles. Simply put, first one starts off with "artificial" or incorrect wavefunctions, to calculate the density. For example, one could use the Hartree wavefunctions.

$$\Psi(\boldsymbol{r}_1, \boldsymbol{r}_2, \boldsymbol{r}_3, \cdots, \boldsymbol{r}_N) = \psi_1(\boldsymbol{r}_1)\psi_2(\boldsymbol{r}_2)\psi_3(\boldsymbol{r}_3)\cdots\psi_n(\boldsymbol{r}_N)$$

and assumes that this gives the exact density

$$n(\boldsymbol{r}) = \sum_i |\psi_i(\boldsymbol{r})|^2.$$

Since the density is exact, according to DFT, it is then possible to express the total energy as a functional of the density

$$E[n] = T[n] + U_{ee}[n] + U_{en}[n] = F[n] + U_{en}[n] \tag{3.15}$$

where $F[n] = T[n] + U_{ee}[n]$ is called the Hohenberg-Kohn functional and is referred to as the universal functional. Unfortunately, we are not able to calculate $F[n]$ because the functional is unknown. However, by adding and subtracting, $\hat{T}_s[n]$ and $\hat{V}_s[n]$ which are the kinetic and interaction energy of the auxiliary wave functions, the expression can be rewritten as

$$\begin{aligned} E[n] &= T[n] + U_{ee}[n] + U_{en}[n] + T_s[n] - T_s[n] + U_s[n] - U_s[n] \\ &= T_s[n] + U_s[n] + U_{en}[n] + \Big(T[n] - T_s[n]\Big) + \Big(U_{ee}[n] - U_s[n]\Big). \end{aligned}$$

These first three terms may be calculated with relative ease. The remaining terms are known as the exchange-correlation (XC) energy

$$E_{xc}[n] = \Big(T[n] - T_s[n]\Big) + \Big(U_{ee}[n] - U_s[n]\Big) \tag{3.16}$$

and they include everything that is not described by $T_s[n]$, $U_s[n]$ and $U_{en}[n]$, i.e., the complex many-electron effects [17]. The DFT still holds, and guarantees that the expression is exact so long as $E_{xc}[n]$ is exact. For a non-interacting system the XC energy is zero, but for a realistic system it is probably tremendously complex since it should be able to describe very intricate many-particle effects for any physical system, like for instance metals, insulators and molecules [17]. For this reason, the exact form of the XC functional is unknown, and we must settle for approximations (to be discussed in the next chapter). The exact total energy may now be expressed as

$$E[n] = T_s[N] + U_s[n] + U_{en}[n] + E_{xc}[n]. \tag{3.17}$$

The next step is utilizing the variational principle introduced earlier, and it is used to find the ground-state total energy, and to obtain many single-electron equations from the many-electron problem. The total energy is minimized by using the Lagrange multiplier method, with the constraint that the wave functions should be orthonormalized. The full derivation can be found in Appendix A.2, and this results in the Kohn-Sham single electron equations

$$\Big(\frac{-\hbar^2\nabla_j^2}{2m_e} + V_{eff}(\boldsymbol{r})\Big)\psi_j^s(\boldsymbol{r}_j) = \epsilon_j^s\psi_j^s(\boldsymbol{r}_j), \tag{3.18}$$

where ϵ_j^s is the eigenvalue of the equation and is often called the KS-eigenvalue and V_{eff} is the effective potential of the system, defined as

$$V_{eff}(\boldsymbol{r}) = V_{en}(\boldsymbol{r}) + V_{xc}(\boldsymbol{r}) + V_H(\boldsymbol{r}), \tag{3.19}$$

where $V_{xc} = \frac{\partial E_{xc}[n(\boldsymbol{r})]}{\partial n(\boldsymbol{r})}$, V_H is describes the electron-electron interaction and is called the Hartree potential, and V_{en} is the external potential, often referred to the nuclear-electron interaction.

By utilizing the equations above, it can be shown that the total energy can be expressed as

$$E[n] = \sum_j \epsilon_j^s - \frac{q^2}{2} \int\int \frac{n(\boldsymbol{r})n(\boldsymbol{r'})}{|\boldsymbol{r} - \boldsymbol{r'}|} d\boldsymbol{r} d\boldsymbol{r'} - \int V_{xc}(\boldsymbol{r})n(\boldsymbol{r})d\boldsymbol{r} + E_{xc}[n], \tag{3.20}$$

where the derivation of this equation can found in Appendix A.2. The missing piece, namely the XC energy as a functional of electron density, will be discussed in the next chapter.

Chapter 4

Practical aspects of DFT

In the previous chapter, we laid down the fundamental basics of DFT. In this chapter, the practical aspects and numerical implementations of DFT will be discussed.

4.1 Approximations to the exchange-correlation energy

As mentioned earlier, the exchange-correlation functional is not precisely known and therefore needs to be approximated. Even so, there have been developed many methods for that purpose, but in this study we will focus on the most popular approximations, that are relevant, and they will be discussed in the following subsections.

4.1.1 The Local Density Approximation

The simplest method for approximating the exchange-correlation energy, is the local density approximation, also known as LDA. It assumes that the exchange-correlation energy, $E_{xc}[n(\boldsymbol{r})]$, can approximated by the exchange-correlation energy of an electron in an homogeneous electron gas of the same density $n(\boldsymbol{r})$.

$$E_{xc}[n(\boldsymbol{r})] = \int n(\boldsymbol{r})\epsilon_{xc}[n(\boldsymbol{r})]d\boldsymbol{r} \tag{4.1}$$

where ϵ_{xc} is the exchange-correlation energy per electron of a homogeneous electron gas of density $n(\boldsymbol{r})$ [20].

As it is the simplest exchange-correlation functional, it accordingly has a few drawbacks. One of them is the incomplete cancellation of the self-interaction term, which leads to a repulsion that may cause artifical repulsion between electrons, and hence increased electron delocalization [21]. In addition, LDA has proven challenging to use when studying atoms and molecules because of their rapidly varying electron densities, however, the LDA is seen as succesful for bulk materials because of the slowly varying electron density [9]. Still, the LDA works surprisingly well for many systems with relatively low computational cost, which makes the LDA an overall good estimation for the exchange-correlation functional.

4.1.2 The Generalized-Gradient Approximation

Another method for approximating the exchange-correlation energy, is the generalized gradient approximation, often shortened down to GGA. The physical idea behind GGA is simple; real electron densities are not uniform, so including information of the gradient of the electron density can create a functional with greater flexibility to describe real materials. In GGA, the exchange-correlation energy, E_{xc}, is expressed using both the local electron density and the gradient of the electron density [9]:

$$E_{xc}[n(\boldsymbol{r})] = \int f(n(\boldsymbol{r}), \nabla n(\boldsymbol{r}))d\boldsymbol{r} \tag{4.2}$$

However, as opposed to LDA, the GGA scheme is not unique. Thus, there is a vast number of possibilities as to which form of the function $f(n(\boldsymbol{r}), \nabla n(\boldsymbol{r}))$ could take. Two widely used GGA functionals are PW91 (Perdew-Wang [22, 23]) and PBE (Perdew-Burke-Ernzerhof [24, 25]). In this project we will utilize PBE as the GGA method.

4.1.3 Van der Waals interactions

Dispersion interactions, also known as van der Waal interactions play an incredibly important role in our everyday lives, especially at the moelcular level. Unfortunately, the approximations to the XC energy we have discussed so far (LDA, GGA) are not able to describe long range non-covalent interactions. Therefore, functionals that can take this into account have been developed, such as vdW functionals. However, there exist several different methods for how to add the vdW corrections into the current DFT approximations. One such method is the DFT-D method where the idea is simply to add a dispersion-like contribution to the total energy

$$E_{Total} = E_{DFT} - S\sum_{i\neq j}\frac{C_{ij}}{r_{ij}^6}f_{damp}(r_{ij}) \tag{4.3}$$

where E_{DFT} is the bare Kohn-Sham energy, r_{ij} is the distance between atoms i and j, C_{ij} is a dispersion coefficient for atom i and j, $f_{damp}(r_{ij})$ is a damping function to avoid unphysical behavior of the dispersion term for small distances [9]. The vdW functionals we will explore in this work are DFT-D3, rev-vdW-DF2 and vdW-opt88.

4.1.4 Hybrid Functionals

To increase the accuracy of DFT, a new type of XC-energy was developed to tackle this issue. The idea was to intermix exact HF exchange with the E_{xc} functionals from LDA or GGA, therefore these kind of functionals were named hybrid functionals. There exists many combinations of LDA or GGA and HF which are different and give rise to different hybrid functionals.

One such hybrid functional was developed by Heyd et al. [26] called HSE, and is expressed as

$$E_{xc}^{HSE} = \alpha E_x^{HF,SR}(\omega) + (1-\alpha)E_x^{PBE,SR}(\omega) + E_x^{PBE,LR}(\omega) + E_c^{PBE},$$

where α is the mixing parameter, and ω is an adjustable parameter controlling the short-rangeness of the interaction. $E_x^{HF,SR}(\omega)$ is the short-range Hartree-Fock exact exchange functional, $E_x^{PBE,SR}(\omega)$ and $E_x^{PBE,LR}(\omega)$ are the short- and long-range components of the PBE exchange functional, and E_c^{PBE} is the PBE correlation functional [26]. Standard values of α and ω are $\frac{1}{4}$ and 0.2, respectively. This gives rise to the functional HSE06, and it has been shown to give good results for most systems. Hybrid functionals are known to produce better results than conventional DFT functionals, but the disadvantage of using hybrid functionals are that they possess a much higher computational cost than the standard DFT functionals.

4.2 Modeling of Materials

A DFT-calculation involves solving the Kohn-Sham single-electron equation, shown in Equation 3.18. This set of equations can be solved self-consistently with an iterative method, which will be explained in the next section. However, to accomplish this, the single-electron wave functions in Equation 3.18 are needed. There exists many methods that try to construct the single-electron wave functions, and in the case of crystalline materials, the Bloch function is a popular way of describing such systems, since it takes into account both the periodicity of a crystal and its finite size. The single-electron wave function using Bloch functions can be written as

$$\psi_{\mathbf{k}}(\boldsymbol{r}) = e^{i\mathbf{k}\boldsymbol{r}} u_{\mathbf{k}}(\boldsymbol{r}), \tag{4.4}$$

where $e^{i\mathbf{k}\boldsymbol{r}}$ is called a plane wave, $u_{n\mathbf{k}}(\boldsymbol{r})$ is known as a Bloch wave and $\mathbf{k}$ is the wave vector. The Bloch wave can be expressed

$$u_{\mathbf{k}}(\mathbf{r}) = \sum_{G} u_{\mathbf{k}+\mathbf{G}} e^{i\mathbf{G}\mathbf{r}} \tag{4.5}$$

which is a sum of plane waves with wave vector $\mathbf{G}$, where $\mathbf{G}$ is a reciprocal lattice vector. Combining the two equations above, one can rewrite the wave function to

$$\psi_{\mathbf{k}}(\mathbf{r}) = \sum_{G} u_{\mathbf{k}+\mathbf{G}} e^{i(\mathbf{k}+\mathbf{G})\mathbf{r}}, \tag{4.6}$$

where the equation is linked with the reciprocal space. Therefore, the Kohn-Sham equation is usually solved in the reciprocal space.

However, the Bloch wave expressed through the plane waves have it's drawbacks. The plane waves are most suited to describe free electrons, so the electrons found in the area far away from the nuclei, such as the valence electrons are described very well. Unlike the electrons found in the areas close to the nuclei, such as the core electrons, which behave differently. This does not mean that the plane waves cannot describe the core electrons, but to be able to do it a large number of plane waves are required, which in turn increases the computational cost of the calculation.

Fortunately there are methods that deal with this problem, and one such method is to use pseudopotentials, which is a effective external potential that treats the inner electrons as frozen, and only focuses on the valence electrons. This method is supported by the fact that the properties of materials are largely dominated by the valence electrons of the atoms and the states of core electrons and the nucleus typically remain unchanged upon going from the isolated atom to the solid. This helps with keeping the computational cost lower, since the number of electrons in a crystal quickly reach very large values as the size of the crystal grows, and by focusing only on the valence electrons, the calculations become much easier to handle [9].

Another method for treating core electrons is the linear augmented plane wave (LAPW) method. The main idea is to divide the space into two regions, where in the region of the valence electrons, plane waves are used to describe them, and in the region of the core electrons another method is used to describe them properly. A method that attempts to take advantage of both the methods mentioned earlier, is the projected augmented wave method (PAW), introduced by Blöchl [27], where it combines features from both the pseudopotential method and the LAPW method.

4.3 The Self-Consistent Field Method

Up until now regarding DFT, we have only discussed the theory behind it and elements that are important for how it is implemented. However, we have not talked about how a calculation is actually performed, and that is what this part will try to explain.

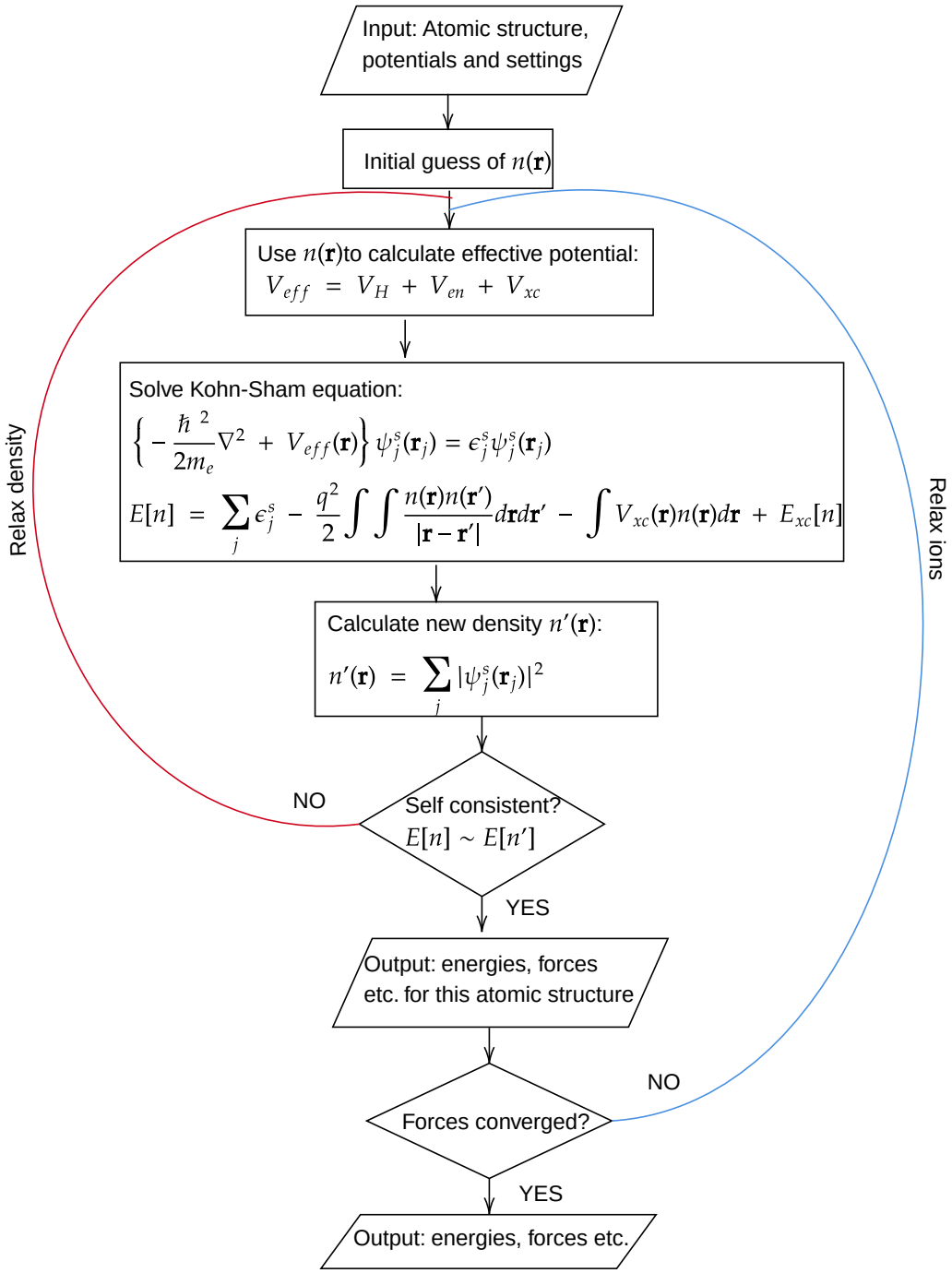

Figure 4.1: Flow chart of the self-consistent field calculation. Illustration adapted from [17].

Firstly, to solve the single-electron equations we need the effective potential V_{eff} of the system, however, the effective potential is depended on the density $n(\mathbf{r})$ of the system, which in turn depends on the wave functions that again depends on the effective potential. The solution to this issue is to use an iterative method, where an initial guess on the density is guessed as illustrated in Figure 4.1. After the initial trial density is suggested, the next step is to calculate the effective potential using the trial density. Afterwards, the single-electron wave functions can be calculated from the Kohn-Sham equation using the effective potential found earlier. Then, using the newly calculated single-electron wave functions, a new density can be formed. Now the newest density is used as a trial density and the procedure is repeated until the minimum energy is obtained and converged. The energy is converged when the last two iterations give the same energy, or in numerical terms, only differ by a set convergence criteria.

After the total energy for the electrons have converged, the focus is shifted towards calculating the positions of the atoms in the structure. This is accomplished by calculating the forces between all the atoms in the structure, and find when the forces acting on the atoms are close to zero, because when that happens, the atoms are in their minimum energy position. To find the energy minimum for the ions in the structure, a numerical method that deals with finding minimums of functions are utilized. There exists many such methods, but two that are widely used are the conjugate gradient method and quasi-Newton method.

4.4 Convergence

Solving the Kohn-Sham equations is computationally heavy, and to do it more efficiently, convergence tests are performed to find the limits that is sufficient to get accurate results, and by doing this, the computational load is reduced.

4.4.1 Energy Cutoff

If we study Equation 4.6 more closely, we observe that determining the wave function for each $\mathbf{k}$ vector involves an infinite sum over the reciprocal lattice vectors $\mathbf{G}$, which in a numerical perspective is not feasible. To combat this issue, the infinite sum is truncated, with respect to the kinetic energy of the plane waves, defined as

$$E = \frac{\hbar^2}{2m_e}|\mathbf{k}+\mathbf{G}|^2, \tag{4.7}$$

where the plane waves with higher energies are considered less significant than the plane waves with lower ones. This means that the infinite sum in Equation 4.6 is truncated to only include plane waves with kinetic energies less than some value known as the energy cutoff

$$E_{\text{cutoff}} = \frac{\hbar^2}{2m_e}G^2_{\text{cutoff}}, \tag{4.8}$$

where the infinite sum is reduced into

$$\psi_{\mathbf{k}}(\boldsymbol{r}) = \sum_{|\mathbf{k}+\mathbf{G}|<G_{\text{cutoff}}} u_{\mathbf{k}+\mathbf{G}}(\boldsymbol{r})e^{i(\mathbf{k}+\mathbf{G})\boldsymbol{r}}. \tag{4.9}$$

To find the energy cutoff that is sufficiently high enough for the system one is studying, convergence tests are performed, where the energy of the system is calculated as a function of the energy cutoff [9].

4.4.2 **k-points**

In a practical DFT calculation, a great deal of work goes into solving integrals over the Brillouin zone. To efficiently evaluate these types of integrals, a method developed by Monkhorst and Pack [28], deals with this problem by choosing and weighting the **k**-points from a given mesh by using the symmetry of the system. The mesh is an evenly spaced grid of **k**-points along the reciprocal lattice vectors of the structure, and is denoted $M_1 \times M_2 \times M_3$, and by taking advantage of the symmetry of the system, the integrals do not need to be evaluated in the entire BZ, but only in a reduced region called the Irreducible Brillouin Zone (IBZ). This means that the number of **k**-points is greatly reduced, which leads to the numerical effort also being significantly lessen. This is all valid when working on bulk structures, but when determining the **k**-points for 2D-structures, the spaced grid of **k**-points can be further simplified into only using one **k**-point in the direction with no surface, due to the electron density tailing off to zero a short distance from the surface. Another thing that should be mentioned is that the integrals solved over the Brillouin zone may sometimes be discontinuous, but there exists methods which deals with these kind of problems, and two common methods are known as the tetrahedron method and the smearing method [9].

To find a sufficient number of **k**-points to use for the system one is working on, convergence tests are performed, where the energy of the system is calculated as a function of the number of **k**-points used in the mesh.

Chapter 5

Computational Details

This chapter contains all the computational details necessary to reproduce the results. The chapter starts with information about the simulation package, choice of XC functional and various settings. Then, convergence tests are presented so that the reader can assess the accuracy of the calculations. Finally, the calculation for the electronic structure and optical properties are discussed, for both the bulk structure and two-dimensional structures.

5.1 Vienna Ab Initio Simulation Package

The Vienna Ab initio Simulation Package often shortened down to VASP (Kresse and Hafner [29, 30], Kresse and Furthmüller [31], Kresse and Furthmüller [32]) is used to perform the calculations in the present work. In this section a brief insight into how calculations are performed with VASP is given, and the settings used in this thesis.

5.1.1 Input Files

Running a simulation in VASP requires four main input files;

- **INCAR**:
  This file contains all the input parameters, that determines how the calculation is initialized, convergence criteria and ultimately how it is executed.
- **POSCAR**:
  This file defines the crystal structure (atomic positions and unit cell parameters) of your structure.
- **KPOINTS**:
  Contains specifications for the k-point mesh projected onto the Brillouin zone. In this file one also specifies where the mesh should be centered within the BZ.
- **POTCAR**:
  Contains information about the pseudopotential used. VASP provides a catalogue containing already calculated pseudopotentials for a large list of elements in the periodic table. Different pseudopotentials can also be chosen for each element.

All VASP files used in this thesis can be found on https://github.com/Moejay10/DFT.

5.1.2 Settings and Functionals

All calculations were performed using the Projector Augmented Wave method [27, 33] as implemented in VASP. The break condition for the electronic SCF-loop was set to 10^{-6} eV, and the Gaussian smearing method was used with a width of 1 meV.

The functionals used in this work was LDA [20], PBE-GGA [34, 35] and variants of vdW functionals such as DFT-D3 [36], vdW-opt88 [37, 38] and rev-vdW-DF2 [39]. In addition, the HSE06 [40] functional was also used in some cases to calculate the bandgap of the different structures.

5.2 Bulk

5.2.1 Convergence Tests

Convergence tests of the total energy with respect to the energy cutoff and the k-point density were performed and are reported for the PBE functional in Table 5.1 and 5.2. The primitive bulk $BaSi_2$ unit cell was used for all the tests. The energy cutoff was varied from 300 to 650 eV, and the results are shown in Table 5.1. At 500 eV, the total energy changes by less than 2 meV, and so the energy cutoff was set to 500 eV for all calculations where the bulk structure was used.

E_{cut}	E_{tot}[eV]	ΔE_{tot}[meV]
300	-110.609	
350	-110.638	29
400	-110.647	9
450	-110.649	2
500	-110.650	1
550	-110.652	2
600	-110.654	2
650	-110.655	1

Table 5.1: Convergence test of the total energy per unit cell of $BaSi_2$ with respect to the energy cutoff.

The total energy was also calculated as a function of the k-point density, which in each direction is defined as the number of **k**-points per unit reciprocal length ($\frac{2\pi}{\text{Å}}$), rounded up to the closest integer. The **k**-point density was varied from 2 to 5, as shown in Table 5.2. The change in total energy is less than 2 meV for the 4x5x3 mesh, and so a k-point density of 5 was used for all calculations where the bulk structure was used.

N_k	mesh	E_{tot}[eV]	ΔE_{tot}[meV]
2	(2x2x2)	-110.702	
3	(3x3x2)	-110.810	108
4	(3x4x3)	-110.808	3
5	(4x5x3)	-110.808	1

Table 5.2: Convergence test of the total energy per unit cell of $BaSi_2$ with respect to the **k**-point density.

5.2.2 Electronic Structure

The electronic structure of a material can be described and analyzed through the materials band structure and density of states. From Section 2.1.4, we know that bands are formed when many atoms come together and form larger structures. The calculation of the electronic band structure involves the total energy of the system being plotted as a function of the wave vector $\mathbf{k}$, which is done in the Brillouin zone. The Brillouin zone of our orthorombic lattice is illustrated in the Figure 5.1.

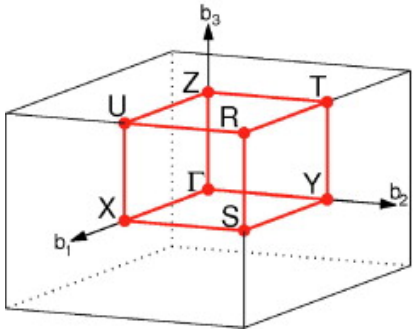

Figure 5.1: Brillouin zone of the orthorombic lattice [41].

Ideally, one would like to know the electron energies in the entire Brillouin zone, but it is computationally heavy, therefore it is more practical to pick out special points and directions in the Brillouin zone, which one can see in Figure 5.1. For our calculations, the high symmetry points chosen was Γ, Y, T, Z, and X.

To help us understand the band structure and more of the materials electronic structure, the density of states is also often calculated. It provides information about the number of electronic states in a given energy interval.

The VASP calculations of the band structure and density of states, involves a two-step process, where the structure has already been relaxed.

- Firstly, a self-consistent calculation is performed.
- In the second calculation step, which is a non-SCF calculation, the calculated density from the previous step is used to calculate the band structure/density of states.

5.2.3 Optical Properties

To study the optical properties of a material, the complex dielectric function is needed. The dielectric function, $\epsilon(E)$, is described as a three-dimensional rank 2 tensor (with components α and β), and defined as

$$\epsilon(E) = \epsilon_1(E) + i\epsilon_2(E), \tag{5.1}$$

where $\epsilon_1(E)$ is the real part and $i\epsilon_2(E)$ is the imaginary part of the complex dielectric function. The imaginary part of the complex dielectric function $\epsilon_2(E)$ can be determined using the following equation

$$\epsilon_2^{\alpha\beta}(E) = \lim_{\mathbf{q}\to 0} \frac{4\pi^2 e^2}{\Omega \mathbf{q}^2} \sum_{c,v,\mathbf{k}} 2w_k \delta(E_c(\mathbf{k}) - E_v(\mathbf{k}) - E) \times \langle u_c(\mathbf{k} + \mathbf{e}_\alpha \mathbf{q}) | u_v(\mathbf{k}) \rangle \langle u_c(\mathbf{k} + \mathbf{e}_\beta \mathbf{q}) | u_v(\mathbf{k}) \rangle^* , \tag{5.2}$$

where $\mathbf{q}$ is the wave number, $u_c(\mathbf{k})$ and $u_v(\mathbf{k})$ are the cell periodic parts of the eigenfunctions for the conduction and valence band with energies $E_c(\mathbf{k})$ and $E_v(\mathbf{k})$, respectively. Ω is the primitive

cell volume, e is the electron charge, w_k is the weight of the **k**-points, and $\mathbf{e}_\alpha$ and $\mathbf{e}_\beta$ are the unit vectors for the three Cartesian directions x, y, and z.

The corresponding real part $\epsilon_1(E)$ of the dielectric function is obtained via the Kramers–Kronig transformation relation

$$\epsilon_1^{\alpha\beta}(E) = 1 + \frac{2}{\pi} P \int_0^\infty \frac{\epsilon_2^{\alpha\beta}(E')E'}{E'^2 - E^2 + i\eta} dE' \tag{5.3}$$

where P is the principal value and η is a sufficiently small number.

The absorption coefficient is determined directly from the complex dielectric function through the relation

$$\alpha^{\alpha\beta}(E) = \frac{\sqrt{2}E}{\hbar c} \sqrt{\frac{\sqrt{\epsilon_1^{\alpha\beta}(E)^2 + \epsilon_2^{\alpha\beta}(E)^2} - \epsilon_1^{\alpha\beta}(E)}{2}}, \tag{5.4}$$

where c is the speed of light [42].

The VASP calculations of the dielectric function were performed in two steps.

- Firstly, a self-consistent calculation is performed.
- In the second calculation step, which is a non-SCF calculation, we used the outputs from the previous SCF calculation and computed the dielectric function, by using the independent particle approximation.

5.3 2D-Layers

5.3.1 Creation of Layers

The construction of a 2D system is done by starting off with the bulk, shown in Figure 5.2, and then insert a vacuum in one of the directions, in this case we have chosen the **a**-direction, illustrated in Figure 5.3.

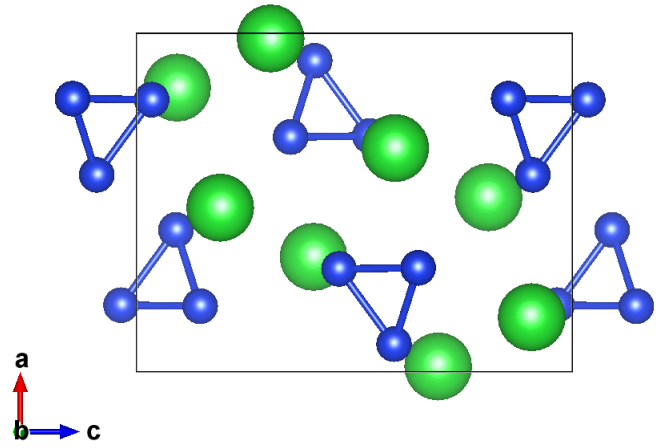

Figure 5.2: The bulk structure of $BaSi_2$. The green spheres represent barium atoms and the blue spheres represents the silicon atoms. This figure is produced using the software VESTA [11].

Figure 5.3 shows a two layer (L2) 2D-structure of $BaSi_2$, where each layer consists of 12 atoms with four Ba-atoms and eight Si-atoms. By adding or removing such layers can we create **n**-layers, where $\mathbf{n} = 1, 2, 3, \ldots$. However, when modelling 2D-materials, one must find how much of a vacuum is needed to simulate the 2D-system. The easy thing one can do is to insert a very large vacuum, but that will be computationally expensive. So in order to find the lowest amount of vacuum needed to simulate the 2D-system, convergence tests are required.

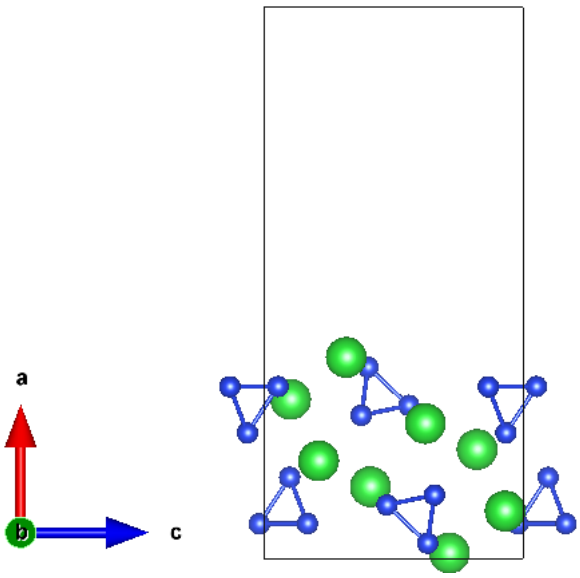

Figure 5.3: The bulk structure with added vacuum in the **a**-direction, Observed from down the **b**-direction. This figure is produced using the software VESTA [11].

5.3.2 Convergence Tests

In the case of the 2D-structures, one firstly has to determine the vacuum thickness of the structure, before doing convergence test of the total energy with respect to the energy cutoff and the k-point density. The two layered $BaSi_2$ unit cell was used for all the tests, using the PBE functional. The vacuum thickness was varied from 2 to 20 Å, and the result are shown below in Table 5.3. At 14 Å, the total energy changes by less than 15 meV, but to be on the safe side, the vacuum thickness was set to 15 Å for all calculations regarding the layered structures.

Vacuum [Å]	E_{tot}[eV]	ΔE_{tot}[meV]
0.0	-81.127	
2.0	-72.414	8713
4.0	-75.326	2912
6.0	-73.155	2171
8.0	-72.622	533
10.0	-72.481	141
12.0	-72.440	41
14.0	-72.426	14
16.0	-72.420	6
18.0	-72.417	3
20.0	-72.415	2

Table 5.3: Convergence test of the vacuum thickness of L2 $BaSi_2$ with respect to the energy difference.

After that was decided, the convergence tests of the total energy with respect to the energy cutoff and the k-point density were calculated. Table 5.4 shows the energy cutoff was varied from 300 to 650 eV, and at 500 eV, the total energy changes by less than 3 meV, and so the energy cutoff was set to 500 eV for all calculations regarding the layered structures.

E_{cut}	E_{tot}[eV]	ΔE_{tot}[meV]
300.0	-72.382	
350.0	-72.409	26
400.0	-72.418	9
450.0	-72.425	7
500.0	-72.426	2
550.0	-72.421	5
600.0	-72.419	2
650.0	-72.418	1

Table 5.4: Convergence test of the total energy of L2 $BaSi_2$ with respect to the energy cutoff.

Table 5.5 shows how the k-point density was varied from 3 to 6. The change in total energy is less than 1 meV for the 1x6x4 mesh, and so a k-point density of 6 was used for all calculations where the layered structure was used.

N_k	mesh	E_{tot}[eV]	ΔE_{tot}[meV]
3	(1x3x2)	-72.428	
4	(1x4x3)	-72.415	13
5	(1x5x3)	-72.418	3
6	(1x6x4)	-72.418	0

Table 5.5: Convergence test of the total energy of L2 $BaSi_2$ with respect to the **k**-point density.

5.3.3 Electronic Structure

The VASP calculations regarding the electronic structure for the 2D-layered structures are mostly the same as for the bulk. However, the electronic band structure calculation differs a little for 2D-materials than the bulk structure. The electronic band structure for 2D-materials are calculated along the points that are in the plane of the 2D-material. In our case we have the vacuum along the **a**-direction, and so the symmetry point X is neglected for the electronic band structure calculation, and the band structure is calculated along the symmetry points Γ, Y, T, Z.

5.3.4 Optical Properties

The optical calculations for a two-dimensional structure was completed in the same manner as for the bulk described before, where the complex dielectric function and absorption coefficient were determined. However, the calculations for the two-dimensional structure will need to take the vacuum into account, and this subsection will explain how that was done.

Firstly, we have the imaginary part and real part of the dielectric functions obtained from the VASP code, just as in the bulk, and we denote them here as $\hat{\epsilon}_2(E)$ and $\hat{\epsilon}_1(E)$, where they have

not taken the vacuum in to account. Our assumption is that the dielectric function is zero in the vacuum region, and by splitting up the imaginary dielectric function in a vacuum region and a non vacuum region, we end up with the expression

$$\hat{\epsilon}_2(E) = \epsilon_2(E) \cdot \frac{V_L}{V} + \epsilon_2^{\text{vac}}(E) \cdot \frac{(V - V_L)}{V}, \tag{5.5}$$

where V is the total volume of the 2D structure and V_L is the volume of the layers, $\epsilon_2(E)$ is the imaginary part of the dielectric function in the non vacuum region and $\epsilon_2^{\text{vac}}(E)$ is the imaginary part of the dielectric function in the vacuum region. This is illustrated in Figure 5.4.

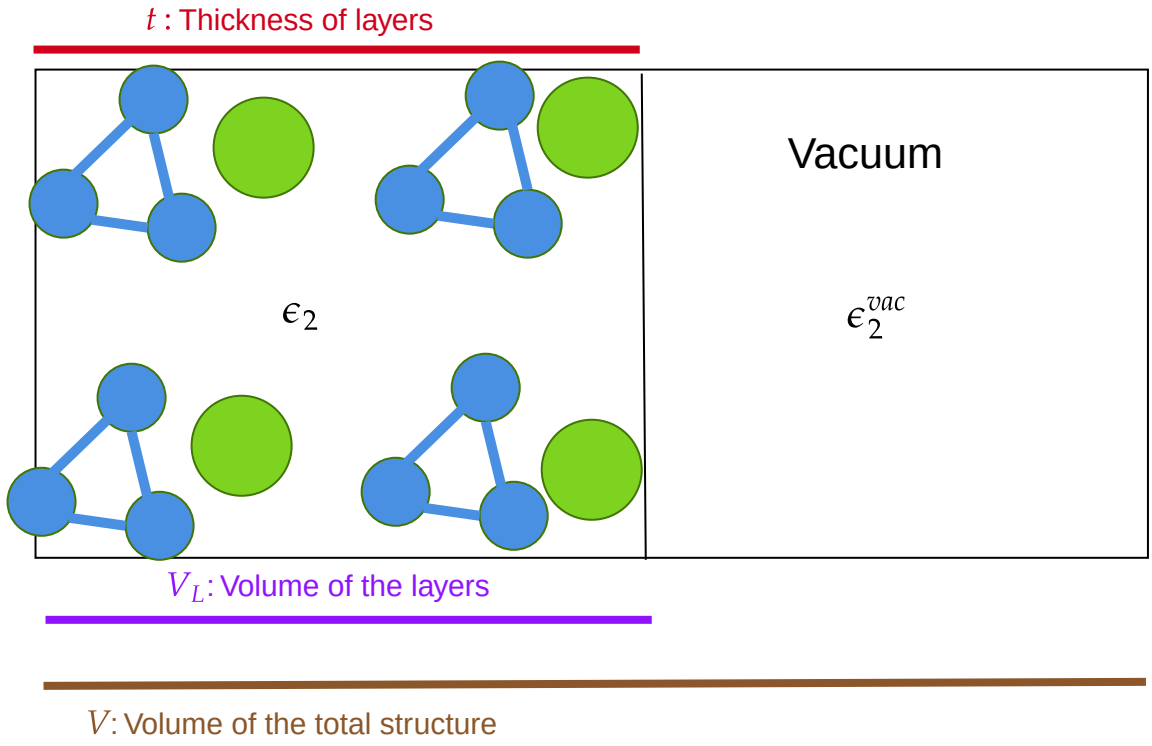

Figure 5.4: Schematic representation of the two layered structure, divided into a vacuum region and non-vacuum region.

We are interested in the imaginary part of the dielectric function which is in the non vacuum region, and since we assumed that the dielectric function is zero in the vacuum, we get that $\epsilon_2^{\text{vac}}(E) = 0$, which modifies the expression above to

$$\hat{\epsilon}_2(E) = \epsilon_2(E) \cdot \frac{V_L}{V} \implies \epsilon_2(E) = \hat{\epsilon}_2(E) \cdot \frac{V}{V_L}.$$

Now we have an expression for the imaginary part of the dielectric function where we have taken the vacuum into account. Furthermore, the total volume of the structure is just the lattice parameters multiplied with each other, $V = a \cdot b \cdot c$, but $V_L = b \cdot c \cdot t$, where t is the thickness of the 2D-structure. That means that the expression for the imaginary part of the dielectric function can be simplified further into

$$\epsilon_2(E) = \hat{\epsilon}_2(E) \cdot \frac{a}{t}. \tag{5.6}$$

With this, we can now find the real part of the dielectric function using the Kramers-Kronig transformation as before

$$\epsilon_1 = 1 + \frac{2}{\pi} P \int_0^\infty \frac{\epsilon_2(E')E'}{E'^2 - E^2 + i\eta} dE' \qquad \text{and} \qquad \hat{\epsilon}_1 = 1 + \frac{2}{\pi} P \int_0^\infty \frac{\hat{\epsilon}_2(E')E'}{E'^2 - E^2 + i\eta} dE' \tag{5.7}$$

$$\epsilon_1 = 1 + \frac{2}{\pi} P \int_0^\infty \frac{V}{V_L} \frac{\hat{\epsilon}_2(E')E'}{E'^2 - E^2 + i\eta} dE' \tag{5.8}$$

$$\epsilon_1 = 1 + \frac{V}{V_L} \Big(\hat{\epsilon}_1(E) - 1 \Big) \tag{5.9}$$

where $\hat{\epsilon}_1(E)$ is the real part of the dielectric function we calculate using VASP and the vacuum has not been taken into account, while $\epsilon_1(E)$ is the real part of the dielectric function, with the vacuum considered. Now we can calculate the absorption coefficient for the 2D structures by using the same expression shown earlier in Equation 5.4, using the real and imaginary part of the dielectric functions where the vacuum has been taken into account.

Chapter 6

Results and Discussion

6.1 Bulk Properties

To be able to understand the results of $BaSi_2$ at the 2D level, it is important to also understand it's properties and behaviour as a bulk structure. Therefore, the respective bulk material $BaSi_2$ have been investigated computationally. Furthermore, to determine which functional to be used when investigating the two dimensional structures, many different functionals have been chosen and compared with each other and available results from the literature, with respect to their structural, electronic and optical properties. To be certain about the selection of the functional, other bulk materials such as $BaGe_2$, which has the same crystalline structure as $BaSi_2$, have also been investigated computationally, to verify the results obtained from bulk $BaSi_2$. The vdW functionals have been included in this study as well, due to the fact that we will be looking at 2D-layered structure afterwards, where van der Waals interactions occur in such systems.

6.1.1 Structural Properties

The relaxed lattice parameters of $BaSi_2$ and $BaGe_2$ are found in Table 6.1. In addition, there are also listed experimental data for some of the materials, regarding $BaSi_2$ and $BaGe_2$.

	BaGe2			BaSi2		
Functional	a [Å]	b [Å]	c [Å]	a [Å]	b [Å]	c [Å]
DFT-D3	9.137	6.828	11.632	8.948	6.709	11.492
LDA	8.907	6.700	11.379	8.759	6.604	11.284
PBE	9.273	6.882	11.740	9.055	6.764	11.588
rev-vdW-DF2	9.092	6.832	11.630	8.906	6.726	11.505
vdW-opt88	9.171	6.873	11.698	8.968	6.761	11.577
HSE06 [12]	9.111	6.854	11.696	8.930	6.752	11.530
Experimental [43]	9.05	6.83	11.65			
Experimental [44]	9.063	6.803	11.63			
Experimental [45]				8.942	6.733	11.555
Experimental [46]				8.92	6.80	11.58

Table 6.1: Lattice parameters of the relaxed unit cell of $BaGe_2$ and $BaSi_2$ obtained from DFT using the DFT-D3, LDA, PBE, rev-vdW-DF2 and vdW-opt88 functionals. The experimental values of $BaGe_2$ (Betz et al. [43], Imai [44]) and $BaSi_2$ (Evers [45], Schäfer et al. [46]), as well as other DFT calculated results using the HSE06 functional (Kumar et al. [12]) are included for comparison.

From table 6.1 we observe that the calculated lattice parameters for both materials are similar to the experimental reported values and to those obtained from hybrid functional calculations. However, when closely studying the performance of each functional individually, we see some clear differences between them. Firstly, let us discuss the performance of the LDA functional. The present work confirms the well-known trend that LDA underestimates lattice constants, and this is observed for both $BaSi_2$ and $BaGe_2$, when compared to the experimental reported values. In the case of the PBE functional, it is well known that GGA-functionals overestimates the lattice constants. This is clearly evident for the material $BaGe_2$, where all the lattice constants are too large compared to the experimental reported values. For $BaSi_2$, this only occurs for the lattice constant a, when we compare the PBE-functional with the experimental reported values.

The lattice parameters obtained from the vdW-functionals (DFT-D3, rev-vdW-DF2 and vdW-opt88), are in good agreement with the experimental reported values, regarding both $BaSi_2$ and $BaGe_2$. In the matter of $BaGe_2$, the vdW-functionals and the hybrid functional performed much better than the conventional DFT functionals PBE and LDA. Moreover, it seems that the hybrid functional obtained from Kumar et al. [12], and the vdW-opt88 functional all have larger values for the lattice parameters for $BaGe_2$, when compared to the experimental values. The lattice parameter values from functional rev-vdW-DF2 and DFT-D3 seems to be closer to the experimental values than vdW-opt88 and hybrid functional. We observe something similar for $BaSi_2$, which is that the lattice parameters calculated by rev-vdW-DF2 functional is lower than the hybrid functional and vdW-opt88 functional.

Overall, when looking at the results of all the functionals for both materials, it seems that the rev-vdW-DF2, vdW-opt88 and HSE06 are in closest agreement with the experimental reported values. Between the rev-vdW-DF2 and vdW-opt88 functional, there is no clear indication from the results which of them performed the best, at least for $BaSi_2$ and this could be due to the larger deviation in the experimental results. Whereas in the case of $BaGe_2$ the rev-vdW-DF2 functional seems to be closer to the experimental results, where the deviation in the experimental results are smaller than for $BaSi_2$.

Since we will be studying 2D-layered structures, a functional that can describe the vdW forces should be chosen, and as we have seen from the results from Table 6.1, vdW forces seems to also be affecting the bulk structures. Therefore, we will primarily consider the vdW functionals for the further study in this thesis. To help us determine which vdW functional we were going to use, we looked at the more thoroughly researched study completed by Tran et al. [47], where they looked into numerous different functionals, including many varieties of vdW functionals. They tested the functionals on countless different types of materials, such as weakly bound solids, namely rare gases, layered systems such as graphite, and molecular solids, but also strongly bound solids. Their findings showed that among the tested functionals, the rev-vdW-DF2 functional was very accurate for weakly bound solids, but also quite reliable for strongly bound solids. In addition, they also mentioned in the paper that rev-vdW-DF2 seemed to produce good results for layered systems such as graphite, which could indicate that it could also work well for other similar structures. From their findings, it seems that rev-vdW-DF2 might be the vdW-functional of choice, and therefore we will use this functional throughout this thesis, to examine the bulk structures and 2D-structures further.

6.1.2 Electronic Structure

Here, we analyze the electronic properties of $BaSi_2$ and $BaGe_2$ by calculating both the electronic band structure and the atomic resolved DOS, and it was calculated from the relaxed unit cell produced by the functional rev-vdW-DF2. The band structure was plotted along the lines connecting the high-symmetry points in reciprocal space $\Gamma - Y - T - Z - \Gamma - X$, which corresponds to the points $\Gamma = (0,0,0), Y = (0,1/2,0), T = (0,1/2,1/2), Y = (0,0,1/2), X = (1/2,0,0)$, and the results are shown in Figure 6.1.

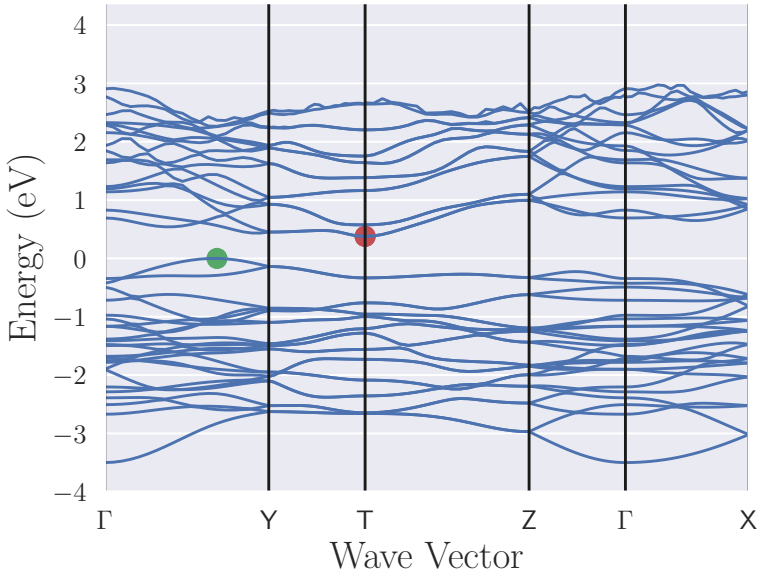

(a) $BaGe_2$

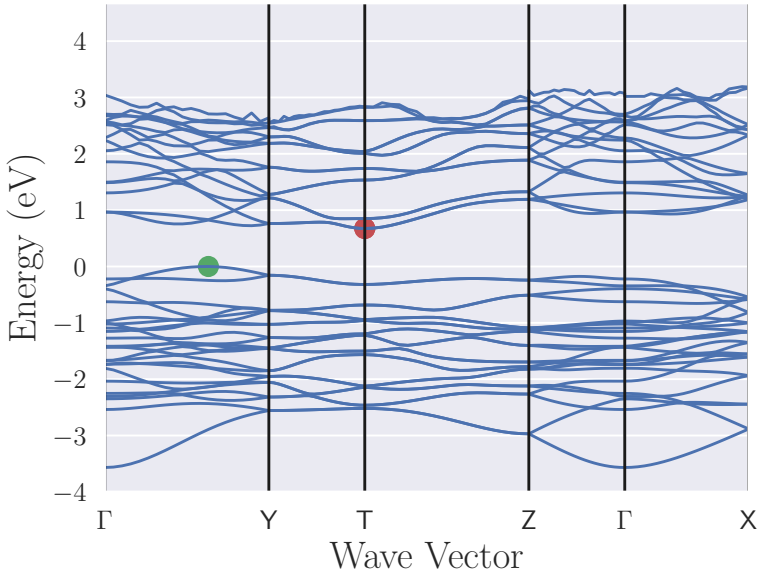

(b) $BaSi_2$

Figure 6.1: Electronic band structure of a) $BaGe_2$ and b) $BaSi_2$ along high symmetry directions, calculated by the rev-vdW-DF2 functional. The VBM and CBM are presented in figure as the green and red point, respectively.

From Figure 6.1, it is easy to observe that both compounds have a similar band structure. Both compounds seems to possess an indirect band gap, since the VBM and CBM is located at different points, where VBM is located along the line between the Γ-point and Y-point, and the CBM is found at the T-point. These findings are in good agreement with the earlier published result from Kumar et al. [12], where they studied both compounds, but instead they used the hybrid functional. However, unlike the small difference of the lattice parameters for the two functionals (rev-vdW-DF2 and HSE06), the difference in the band gap energy is quite significant. Table 6.2 shows the calculated band gap energies, where they are also compared to experimental data.

Table 6.2: Fundamental band gap (E_g) and lowest direct band gap (E_g^{dir}) in the unit eV, together with the available experimental data. Energies were estimated using the rev-vdW-DF2 functional and the HSE06 functional (in parenthesis).

	E_g	E_g^{dir}	E_g (**Exp**)
$BaGe_2$	0.38 (0.74)	0.56 (0.93)	0.97-1.0 [1]
$BaSi_2$	0.67 (1.12)	0.82 (1.28)	1.1-1.3 [2]

[1] References [48, 49]
[2] References [50, 51, 52, 53, 54, 55]

The hybrid functional seems to be in better agreement with the experimental data for both compounds, than the rev-vdW-DF2 functional, which underestimates the band gap energy by a large margin. These results agree with the literature found in DFT, where conventional DFT functionals suffers from delocalization error, which is responsible for underestimation of band gap energies for materials. The reason hybrid functionals are known to improve the band gap energies of materials, comes from the mixed Hartree-Fock exchange which rectifies some of the issues found in conventional DFT. However, this improved accuracy comes at a price, which is that hybrid calculations are progressively more resource demanding than conventional DFT calculations. The smallest direct band gap E_g^{dir}, which is located near the VBM, is only ~ 0.2 eV higher than the fundamental band gap. It is also often referred to as the optical band gap, and it is important when working on the optical properties. We will discuss it more in the section dealing with the optical properties. The band gaps of both compounds makes them applicable in solar cells, where it is desirable for materials in solar cells to have a band gap energy between 1.0 and 1.5 eV, according to Shockley and Queisser [56].

To understand the contribution of different orbitals to the electronic states in $BaSi_2$ and $BaGe_2$, the atomically resolved density of states were calculated and presented in Figure 6.2. Both compounds seems to exhibit the same properties in the valence band area, where it is dominated by the Si/Ge -p states in $BaSi_2$ and $BaGe_2$, respectively. Furthermore, the contribution from the Ba-p states are also visible in the valence band region, concerning both materials. In the lower energy region of the valence band, we also observe a big contribution from the Si/Ge sp-states at approximately 6 eV below the VBM, with a small contribution from the Ba p-states. This is also what the Kumar et al. [12] found in their study of the materials when utilizing the hybrid functional. However, in the conduction band, the result for $BaGe_2$ obtained by rev-vdW-DF2 and the hybrid functional by Kumar et al. [12] are different. The results from the rev-vdW-DF2 functional tells us that both the Ba-d state and Ge-p state contribute the most in that region, but the results published by Kumar et al. [12] shows that the Ba-d states contributed the most, and then followed by Ge-p states. In the case of $BaSi_2$, the rev-vdW-DF2 seems to be in good agreement with the results found in the paper by Kumar et al. [12], regarding the conduction band area, where Ba-d state contributes the most with a smaller contribution from Si-sp states.

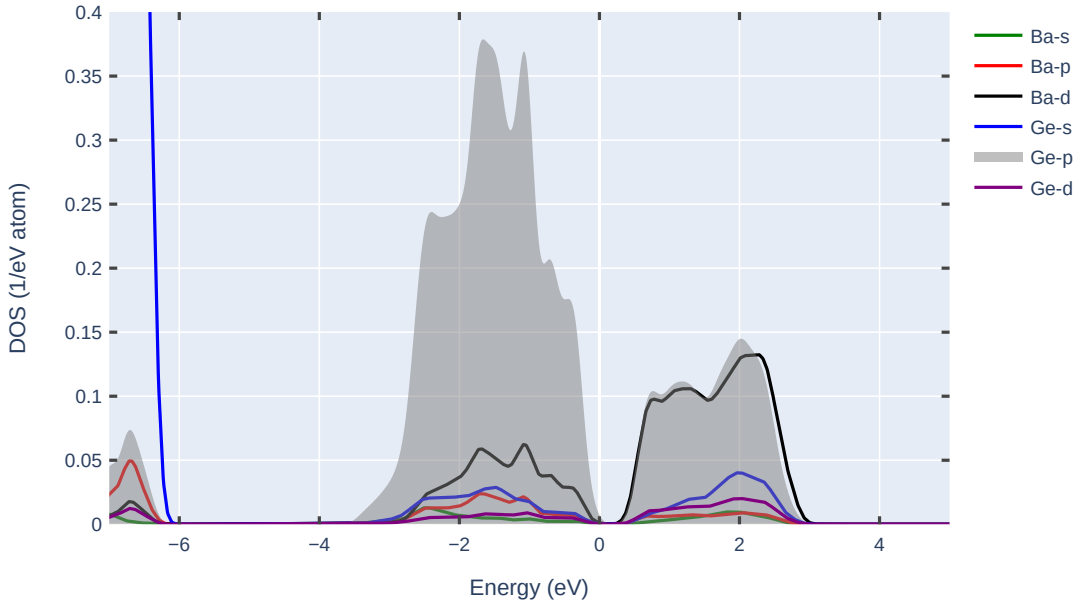

(a) $BaGe_2$

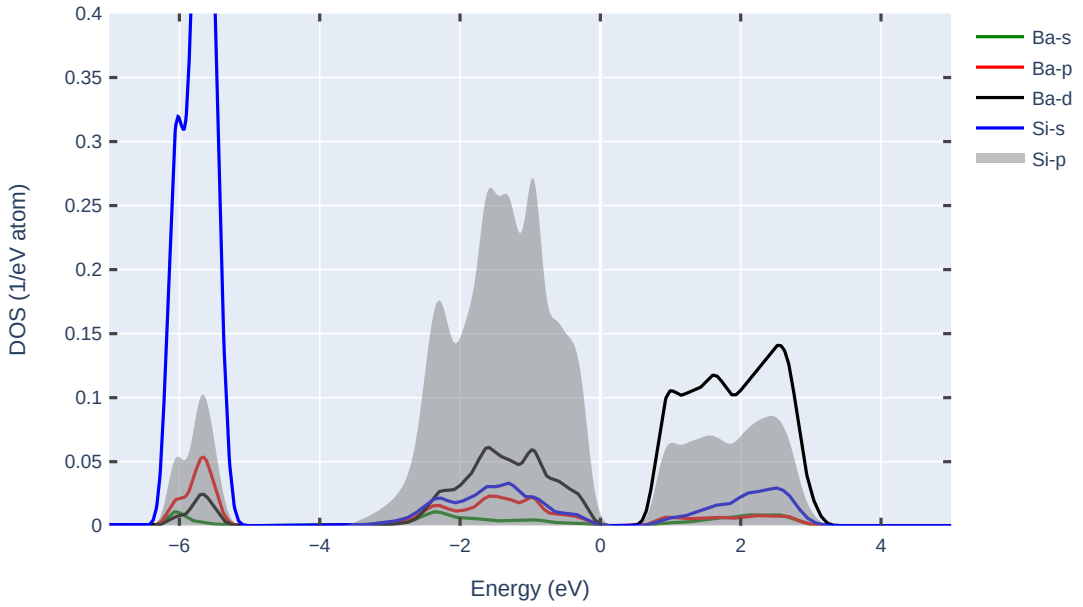

(b) $BaSi_2$

Figure 6.2: Atomically resolved DOS of a) $BaGe_2$ and b) $BaSi_2$. The zero of the absolute energy is set to the VBM.

6.1.3 Optical Properties

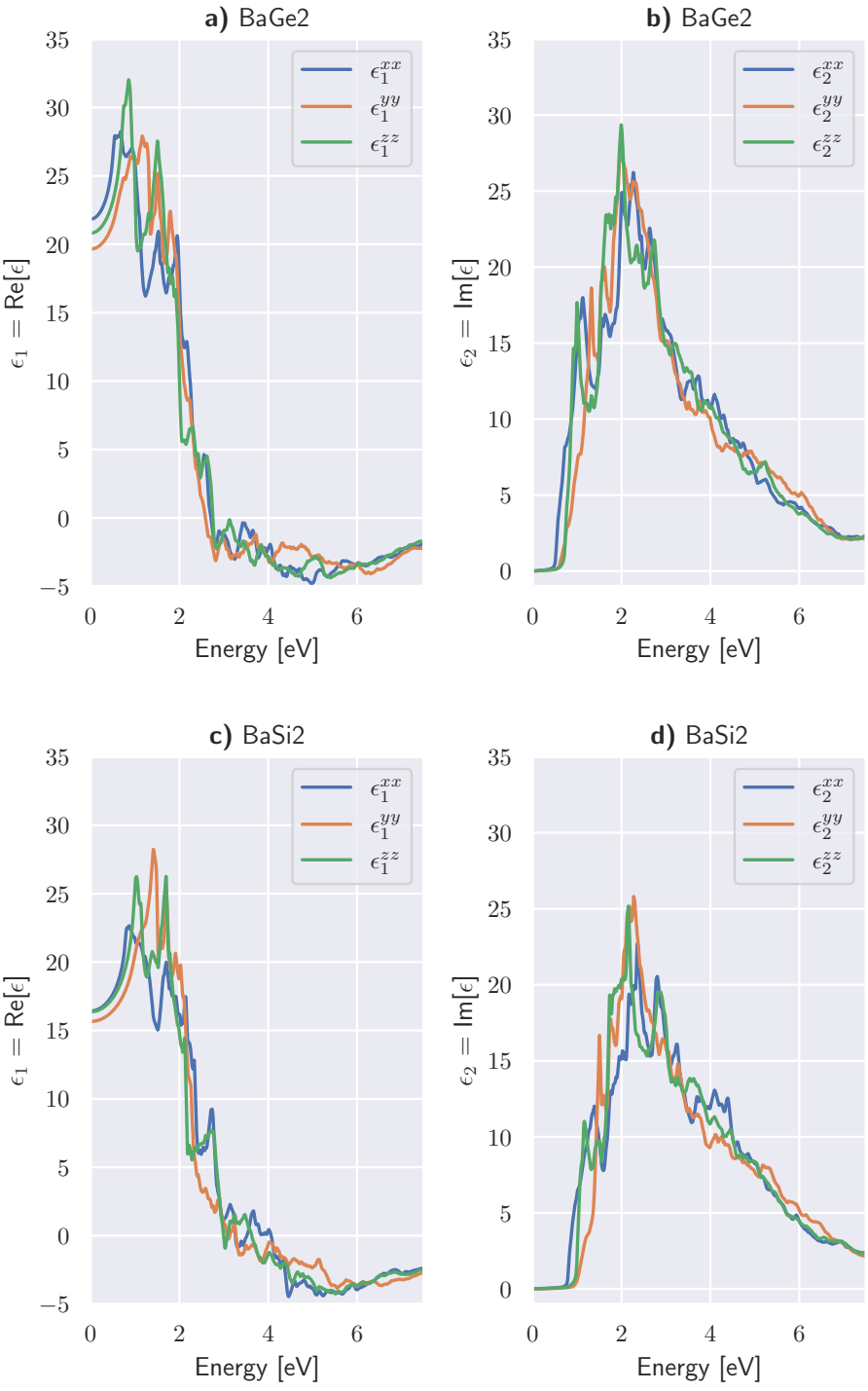

Figure 6.3: The components of the real and imaginary dielectric function, plotted against the photon energy across the xx, yy, and zz tensors, for $BaGe_2$ and $BaSi_2$. The left-hand panels show the real part ϵ_1 and the right-hand panels show the imaginary part ϵ_2 of the dielectric function.

Figure 6.3 displays the real (left figure) and imaginary parts (right figure) of the dielectric function,

and it shows that the two compounds exhibit weak anisotropy in both the real and imaginary parts of the components $\epsilon^{xx}(E), \epsilon^{yy}(E)$, and $\epsilon^{zz}(E)$. $BaGe_2$ and $BaSi_2$ also seems to have similar dielectric response spectra, which could be due to the fact that both materials share a similar electronic structure and that the dielectric function depends on the electronic structure of the material. These results are in good agreement with the findings of [12]. Furthermore, if we observe ϵ_2 a little closer, we see that it is zero up until a certain energy, and that energy is the optical band gap energy, which was presented in Table 6.2.

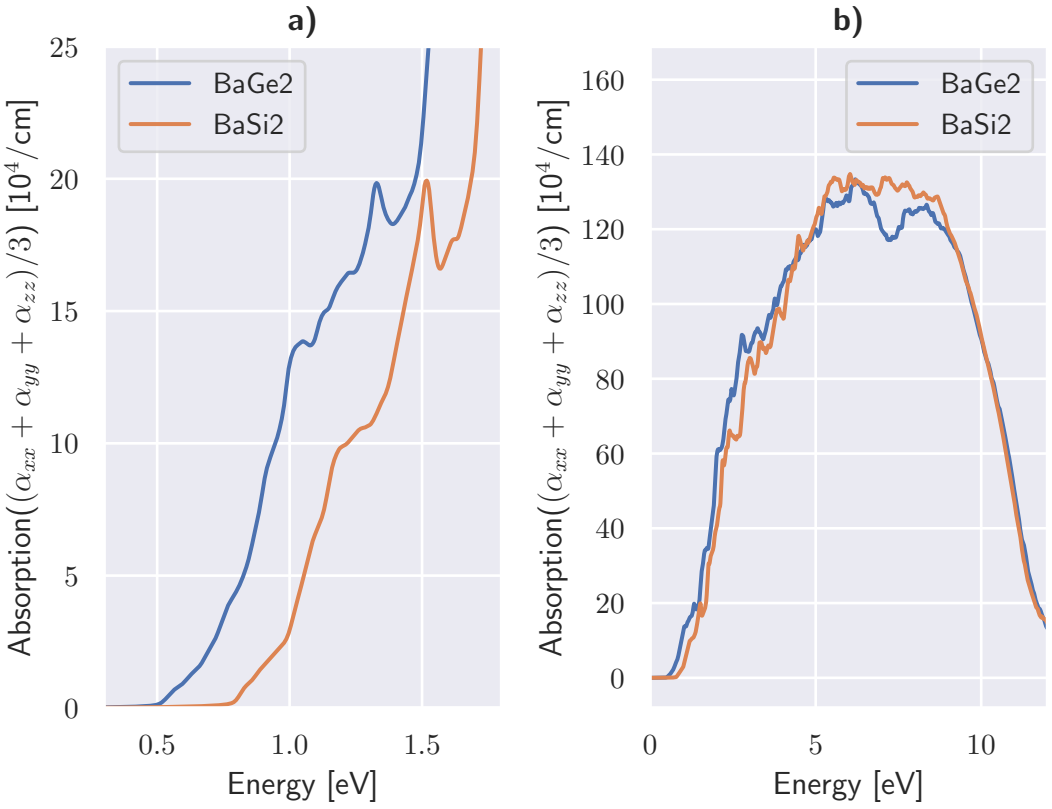

Figure 6.4: The averaged absorption coefficient of $BaSi_2$ and $BaGe_2$ are plotted against the photon energy, where a) shows the onset absorption region and b) shows the absorption over a broader energy region.

The average polarization-independent absorption coefficient, defined as $\alpha(\omega) = (\alpha^{xx}(E) + \alpha^{yy}(E) + \alpha^{zz}(E))/3$, is seen plotted against the photon energy in Figure 6.4. As explained in the previous chapter, the absorption coefficient is directly obtained from the dielectric function, so the anitrosopy we observed for the dielectric function, was also observed for the absorption coefficient. Another thing that is similar between the absorption coefficient and the dielectric function is the onset of energy for $\alpha(E)$ and $\epsilon_2(E)$, where the onset depends on the optical band gap. This is easily observed in Figure 6.4, especially for $BaGe_2$ that has an onset absorption around 0.5 eV and the optical band gap energy was 0.56 eV. Figure 6.4 also shows that both compounds have a similar absorption coefficient, and the only difference is the onset absorption, which is due to the materials having different optical band gap energies. Kumar et al. [12] had the same result, but the onset of absorption between rev-vdW-DF2 and that of HSE06 was different, and that is because the calculation of the optical band gap energy was not the same for both functionals. We observe from Figure 6.4 that both materials seem to have a peak absorption at 4-6 eV, while the results by Kumar et al. [12] reported having a peak absorption at 6-8 eV.

Furthermore, the absorption coefficient of $BaSi_2$ was measured experimentally and reported to be approximately $> 10^4 cm^{-1}$ [57, 58, 59, 60], which is confirmed by our results and the study conducted by [12].

6.2 Monolayer

6.2.1 Stability

L1 - Structures	b [Å]	c [Å]	$E_{tot}[eV]$	E_f/atom[meV]
Unrelaxed	6.778	11.602	-41.277	620.0
R_1	6.423	11.284	-42.373	529.0
R_2	5.717	11.649	-43.088	469.0

Table 6.3: Lattice parameters, total energy and the exfolation energy for the monolayer is presented, where three different possible structures of the monolayer is compared. One is unrelaxed, while the two other monolayer structures R_1 and R_2 have been relaxed using their respective methods, quasi-Newton and conjugate gradient.

Table 6.3 shows the lattice parameters, the total energies and the exfoliation energies for different monolayer structures, where we have included the results for the unrelaxed structure of the monolayer, as well as two different methods of relaxations of the monolayer. The difference between R_1 and R_2 comes from how the calculation was performed, where in the case for R_1 the results was obtained using the quasi-Newton method, whereas the results for R_2 was obtained using the conjugate gradient method. These two methods are used to relax the ions into their groundstate. Looking at the total energy, it is clearly evident that the relaxation done by using the conjugate gradient method gives a lower energy, which means that that the quasi-Newton method found a local minima, which we could think of as a metastable system. This is not a surprise, since the conjugate gradient method usually is better at finding global minimums than the quasi-Newton method, which works best for systems that has a good initial positions. However, when we look at the structural data from the two relaxations, which is illustrated in Figure 6.5, something interesting can be observed.

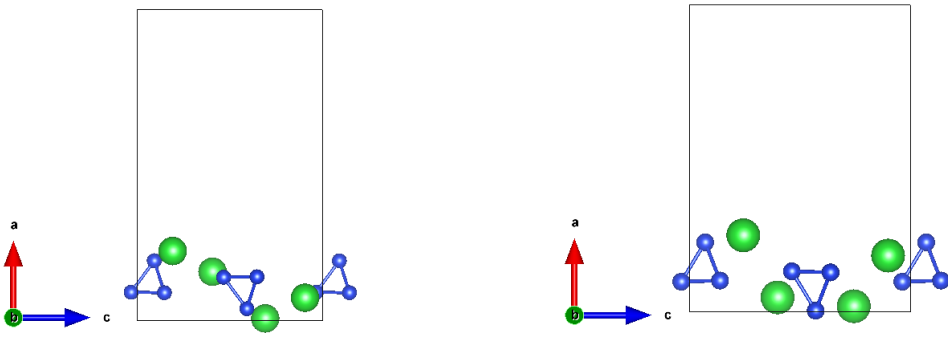

(a) (b)

Figure 6.5: The structural model of $BaSi_2$-monolayer, where we are looking down on from the *b*-axis. The result for quasi-Newton is shown in a) and the conjugate gradient method is illustrated in b).

The system that was relaxed by using the conjugate gradient method seems to have been reconstructed, where several of the barium atoms have shifted their positions by a large margin compared to the unrelaxed system. This does not occur in the system relaxed by using the quasi-Newton method. The result of the relaxation by using the conjugate method seems to suggest that the monolayer of $BaSi_2$ is not a stable structure, but could this have been known in advance?

It turns out that it could have, according to the paper by Choudhary [61], where they studied 2D materials, and suggested a method to identify possible 2D materials that are vdW bonded from their bulk counterparts. Their method used the lattice constants from the PBE calculated results for the bulk in non-cubic crystal systems and compared them with available experimental data. The formula they used was

$$\delta = \frac{|l_{PBE} - l_{ICSD}|}{l_{ICSD}},$$

where δ is the relative difference between ICSD (experimental data) and PBE (DFT calculations using the PBE functional), and l is the lattice constants. By utilizing this method they were able to identify many possible 2D materials. They suggested that a δ greater than or equal to 5% as the screening criterion, however they discussed the possibility that even δ as low as 3.5% can be used as the screening criteria.

By implementing their method on our material $BaSi_2$, we end up with the values presented below.

	δ_a	δ_b	δ_c
Experimental [45]	1.3%	0.5%	0.3%
Experimental [46]	1.5%	0.5%	0.1%

Table 6.4: The relative difference between the lattice parameters calculated using the PBE-functional for the bulk system of $BaSi_2$ and the experimental values by Evers [45], Schäfer et al. [46].

Table 6.4 showcases the relative difference between the experimental data for $BaSi_2$ and the DFT calculated results using the PBE-functional which was presented earlier in Table 6.1. We observe that the relative difference, δ, is nowhere near 3.5% and even further away from 5%, which does suggest that $BaSi_2$ may not be an ideal 2D-structure, at least not as a monolayer.

What if we instead use the metastable system calculated by the quasi-Newton method, maybe that has a possibility as a 2D-structure? The paper by Choudhary [61] also had another way of studying the stability of a 2D material, and that was through the exfoliation energy. They defined the exfoliation energy for 2D materials as

$$E_f = \frac{E_{1L}}{N_{1L}} - \frac{E_{bulk}}{N_{bulk}} \tag{6.1}$$

where E_{1L} and E_{bulk} are the energies of the single layer and 3D bulk material, respectively. Whereas N_{1L} and N_{bulk} are the number of atoms in the single layer and bulk system. The criterion to predict the feasibility of a 2D material using the exfoliation energy was set at 200 meV/atom, and the exfoliation energy of the different monolayers, which can be seen in Table 6.3, had all higher exfoliation energy than the criteria of 200 meV/atom. These results seems to suggest that the $BaSi_2$ might not be a material that is suitable as a 2D material, at least not as a monolayer according to the findings by Choudhary [61].

6.3 Multilayer

6.3.1 Structural Properties

Structure	b [Å]	c [Å]
L2	6.540	11.248
L3	6.617	11.344
L4	6.644	11.388
L5	6.660	11.409
L6	6.671	11.425
L7	6.677	11.436
L8	6.685	11.446
L9	6.687	11.452
L10	6.691	11.456
L11	6.694	11.461
L12	6.696	11.464
L13	6.698	11.466
L14	6.700	11.469
L15	6.701	11.474
L16	6.702	11.475
L17	6.703	11.476
L18	6.705	11.478
L19	6.705	11.479
L20	6.706	11.479
Bulk	6.726	11.505

Table 6.5: The lattice parameters for the 2D layered structures of $BaSi_2$, for the two layered system up to the twenty layered system. For the sake of comparison, the bulk values are also presented. Vacuum is along a-direction and is therefore not included.

Table 6.5 shows the lattice parameters for the different multilayered structures of $BaSi_2$. The 2D multilayered structures did not have the same problem of reconstruction as the monolayer. Figure 6.6 illustrates the 2D multilayered systems for the two layered, three layered, four layered and fifth layered struture.

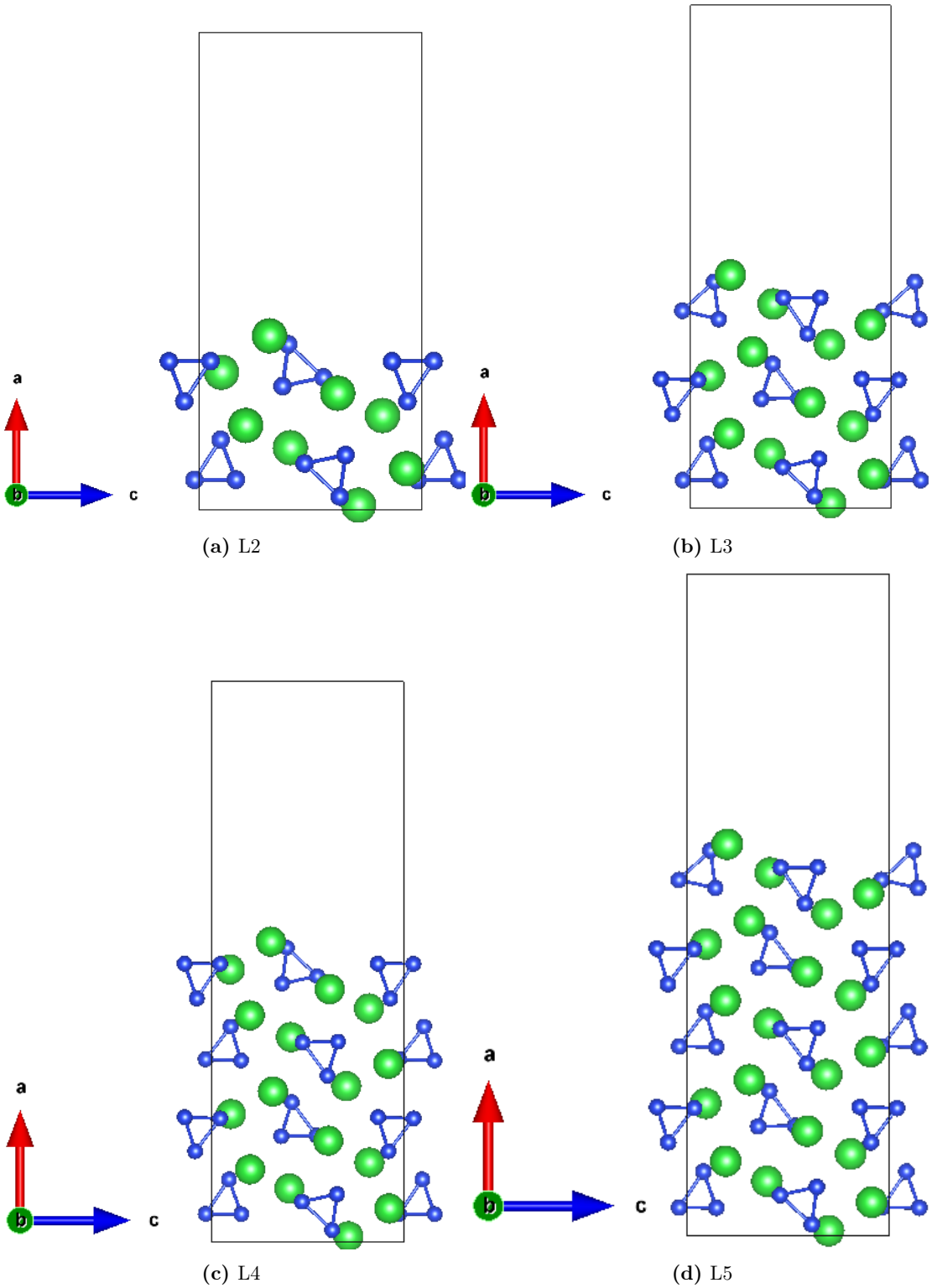

(a) L2 **(b)** L3

(c) L4 **(d)** L5

Figure 6.6: The structural model of 2D-layered $BaSi_2$, where we are looking down on from the *b*-direction for the a) two layered system (L2), b) three layered system (L3), c) four layered system (L4) and d) fifth layered system (L5).

To visualize the result of Table 6.5, the values have been plotted and shown in Figure 6.7, where it is easy to see that when the number of layers increase in the system, the lattice parameters b and c increases, and they seem to almost converge to the bulk's lattice parameters.

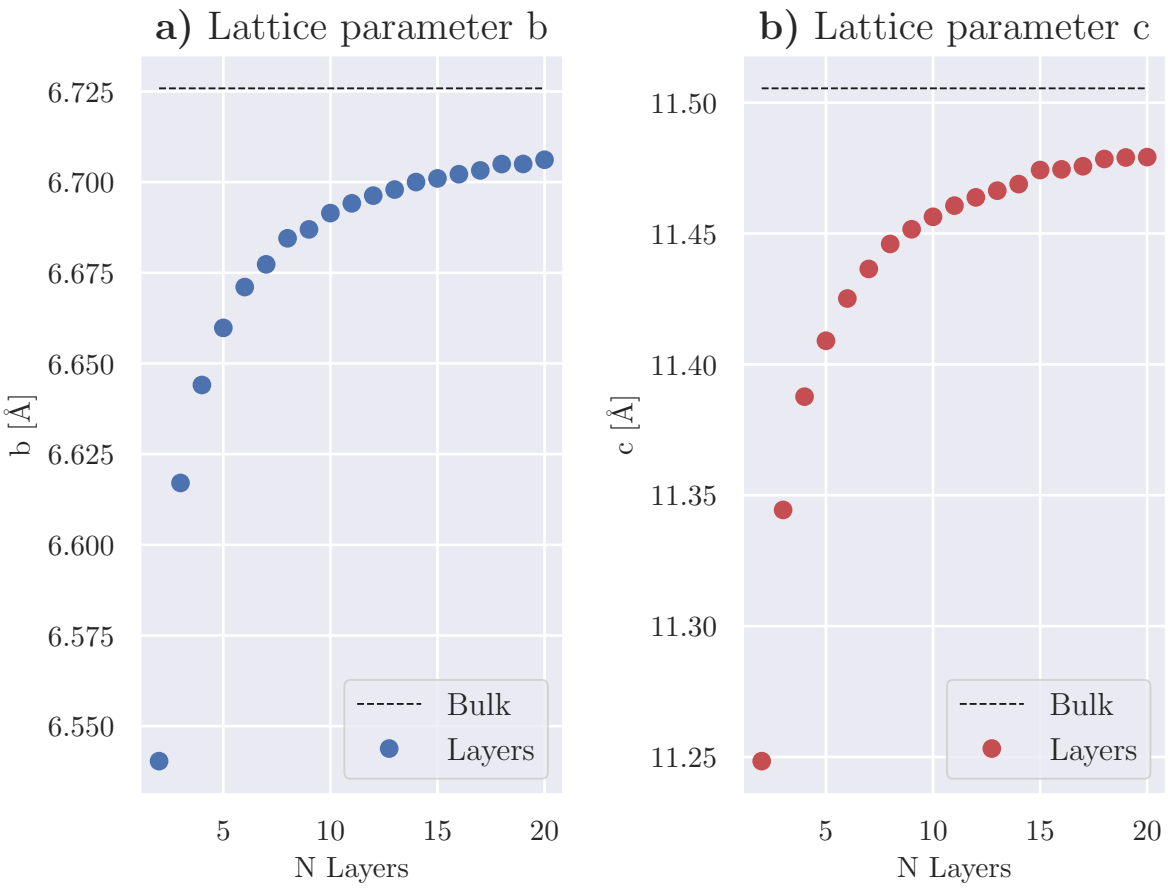

Figure 6.7: The lattice parameters for the 2D layered structures of $BaSi_2$, for the two layered system up to the twenty layered system, which was plotted against the number of layers. The dashed line is the bulk's lattice parameters, shown for comparison.

To understand more of the 2D layered structure, we calculated the total energy of the system per atom, decomposition energy, cohesive energy and exfoliation energy of the 2D layered structures, and the results are shown in Figure 6.8. They are also compared to the bulk's values.
The decomposition energy and cohesive energy are two new terms we have just introduced. The cohesive energy represents a measure of the bonding strength in a structure, where it is the energy required to separate an atom from the structure. Since our structure consists of both barium and silicon atoms, the cohesive energy will instead be the energy required to separate both a single barium and silicon atom from the structure. The cohesive energy E_{coh} is calculated by using following equation:

$$E_{\text{coh}} = E_{\text{tot}}(\text{BaSi}_2) - \mu(\text{Ba}) - 2\mu(\text{Si}).$$

Here, $E_{\text{tot}}(\text{BaSi}_2)$ is the total energy of the layered or bulk structure, $\mu(\text{Ba})$ and $\mu(\text{Si})$ represent the energy of the sole atoms, which was also calculated by using the rev-vdW-DF2 functional. The decomposition energy is somewhat similar to the cohesive energy, the only difference is that instead of $\mu(\text{Ba})$ and $\mu(\text{Si})$ being the energy of the sole atoms, they are the energy of the solid structure of Ba and Si. This was also calculated by using the rev-vdW-DF2 functional.

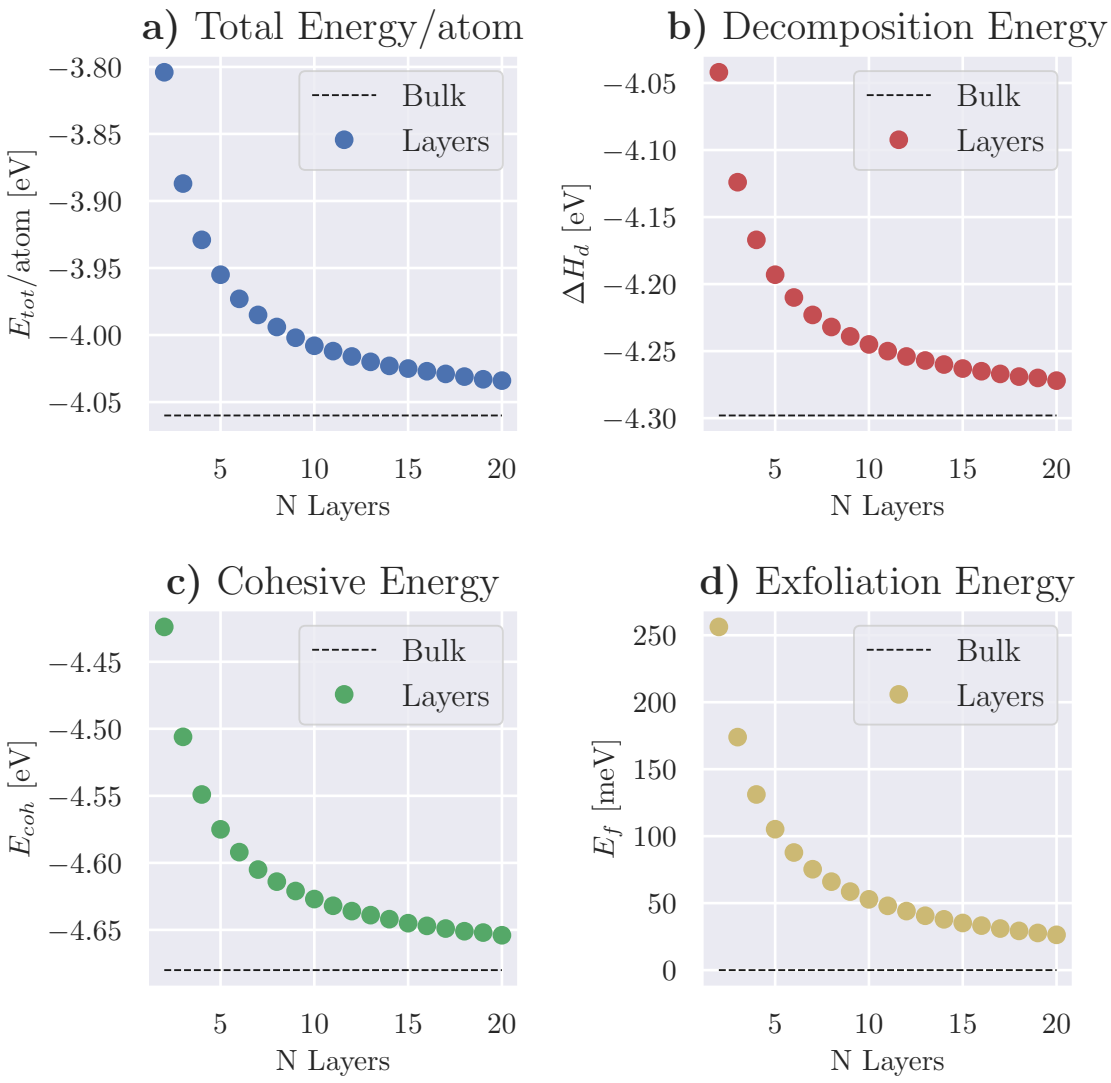

Figure 6.8: Different energy calculations for the 2D layered structures of $BaSi_2$, for the two layered structure up to the twenty layered structure. The dashed line is the bulk's values, shown for comparison.

From the figures above we see a clear trend where the energies of the layers seem to converge against the bulk energy values, and this is observed regarding all energies. This is the same trend we observed for the lattice parameters. Also, in the paper of Kumar et al. [12], they determined $BaSi_2$ to be thermodynamically stable, and since the 2D layered structures become more and more similar to the bulk as the layers increase in the 2D structure, it seems reasonable to assume that the 2D layered structures become more thermodynamically stable as the number of layers increases in the structure. This assumption fits well with the results concerning the decomposition energy and the cohesive energy, where as the number of layer increases in the 2D structure, it becomes more similar to the bulk, and the energy needed for the 2D layered structure to break down increases.

6.3.2 Electronic Structure

Here, the electronic properties of the layered system of $BaSi_2$ will be discussed, where the electronic band structure and the atomic resolved DOS is presented.

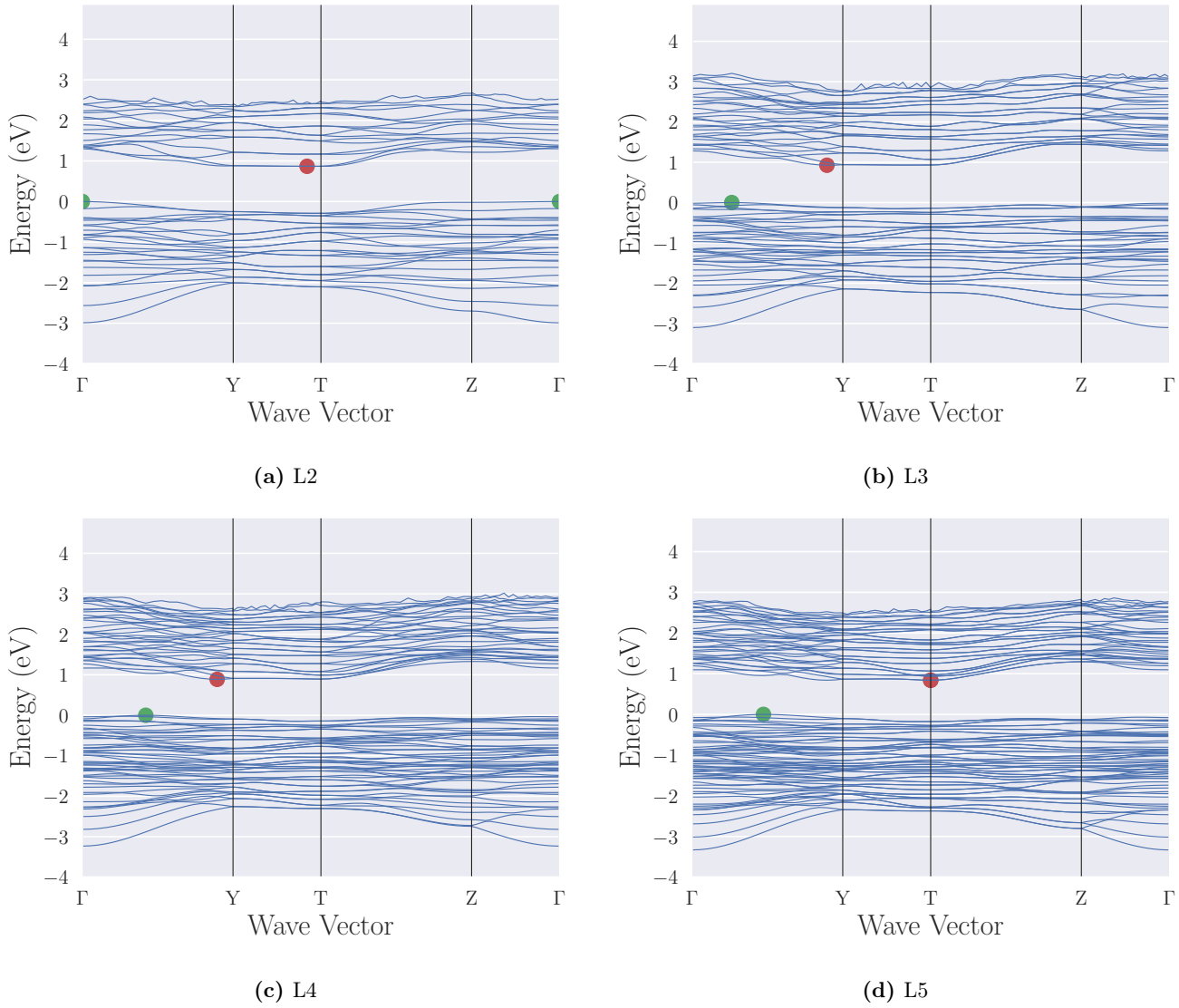

(a) L2 **(b)** L3

(c) L4 **(d)** L5

Figure 6.9: Electronic band structure of a) L2, b) L3, c) L4 and d) L5 along high symmetry directions, calculated by the rev-vdW-DF2 functional. The VBM and CBM are presented in figure as the green and red point, respectively.

Figure 6.9 shows the electronic band structure for the 2, 3, 4 and 5 layered 2D system. The result for the band structure were plotted along lines connecting high-symmetry points in reciprocal space Γ-Y-T-Z-Γ. The first thing to notice is that the layered structures also possess an indirect band gap, just as we saw for the bulk. However, the location of the VBM and CBM seems to change depending on the layer thickness. The location of the VBM and CBM in the L5 system seems to be the same as for the bulk, where the VBM was located along the between the Γ-point and Y-point, whereas the CBM was located at the T-point. This was also observed in the electronic band structure for the thicker layers. Another interesting result regarding the electronic structure is the band gap energy of the 2D layered structures, where Figure 6.10 shows the band gap energy for each layer plotted against the number of layers of the 2D structure.

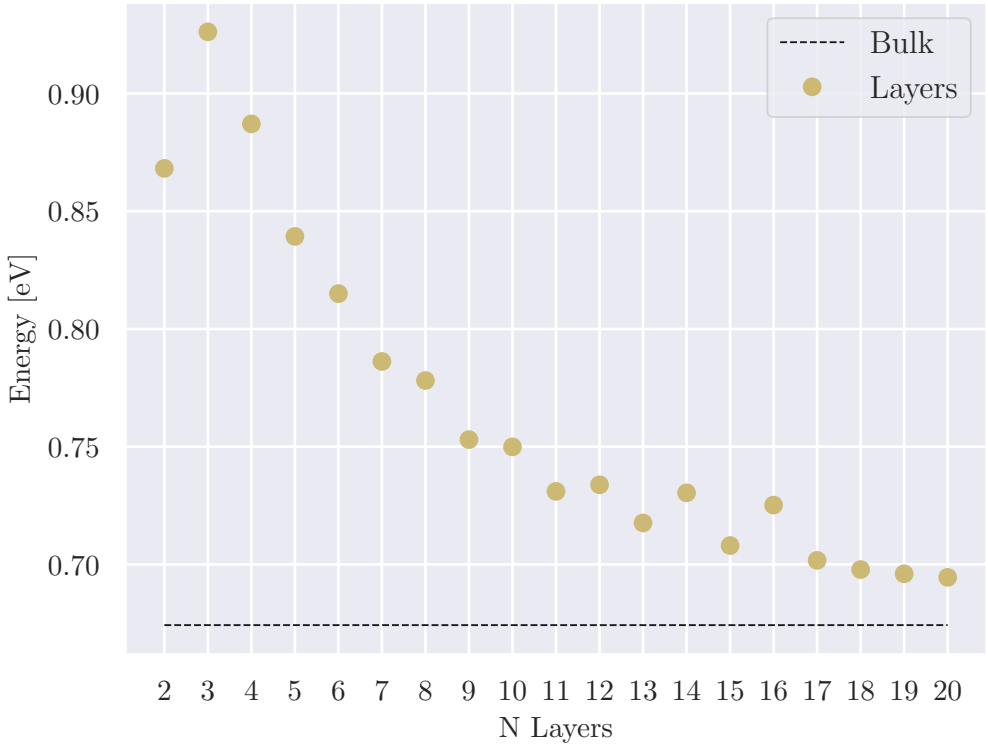

Figure 6.10: The fundamental band gap energy for the two layered structure structure up to the twenty layered structure, extracted from the electronic band structure. The bulk's band gap energy has been added as a comparison.

We observe from Figure 6.10 that the fundamental band gap energy seems to converge towards the bulk's value when the number of layer that build up the layered system is increased. There does seem to be a bit of fluctuations of the fundamental band gap energy for the layered systems, but the trend is that it is converging towards the bulk. This seems to suggest that the layered system upon addition of consecutive layers, is converging to the bulk's electronic band structure. The same phenomenon was also observed when we looked at the lattice parameters and the energy calculations. From the earlier discussion we had about the band gap energy for the bulk, we know that the the rev-vdW-DF2 functional underestimates the band gap energy, and that hybrid functionals are more suited for these kind of calculations. Therefore, we have also calculated the band gap energy using the HSE06 functional on the layered structures. However, due to the calculations being much more computationally demanding, only layered structures from L2-L5 was calculated. The result of this is shown in Table 6.6

Table 6.6: Fundamental band gap (E_g) and lowest direct band gap (E_g^{dir}) in the unit eV for the two layered structure up to the five layered structure. The bulk's band gap energy has been added as a comparison. Energies were estimated using the rev-vdW-DF2 functional and the HSE06 functional (in parenthesis).

	E_g	E_g^{dir}
L2	0.868 (1.319)	1.30 (1.76)
L3	0.926 (1.406)	1.17 (1.66)
L4	0.887 (1.352)	1.04 (1.51)
L5	0.839 (1.301)	0.95 (1.43)
Bulk	0.67 (1.12)	0.82 (1.28)

Table 6.6 shows that the band gap energies for the layered structures from both the rev-vdW-DF2 and HSE06 functional shares the trend of the band gap energy decreasing after the L3 structure. This means that even though the rev-vdW-DF2 does not calculate the correct band gap energy, it can tell us the trend of it, and what we have observed is the fact that the band gap energy is dependent on the thickness of the layered structures. A similar trend was reported in the paper by David K. Sang [62], where they looked into the two-dimensional structure of Te. Moreover, the band gap energies for the 2D layered systems L2-L5 seems to be in the suitable band gap range of 1.0-1.5 eV as per Shockley-Queisser criterion [56], and the fact that the band gap energy can be changed depending on the thickness of the 2D-structure, makes the 2D layered structures interesting in applications within solar cells. In the case of E_g^{dir}, which was located near the VBM, it is only ~ 0.2 eV higher than the fundamental band gap energy, but that only applies for the L3-L5 structures, and not the L2 structure, where the difference is around ~ 0.4 eV. It will be discussed more in the section of optical properties.

To further understand the contribution of the different orbitals to the electronic band structure in the layered structures of $BaSi_2$, the atomically resolved density of states have been calculated based on the rev-vdW-DF2 functional and is presented in Figure 6.11. Only the density of states for L2-L5 is shown. The DOS of the L2 to L5 structures are similar to the DOS of the bulk, shown in Figure 6.11, where in the valence band area, the Si-p states is contributing the most, followed by the Ba-d and Si-s states. They are also similar in the lower energy region of the valence band at approximately 6 eV below the VBM, where the area is dominated by the Si-sp orbitals. We observe the same for the DOS in the conduction band area, where the Ba-d orbitals are dominating, and Si-p orbitals comes in second. Similar results were observed for all the thicker layers, and the only difference was the number of states involved in the DOS, which is due to the difference in atoms in the structures.

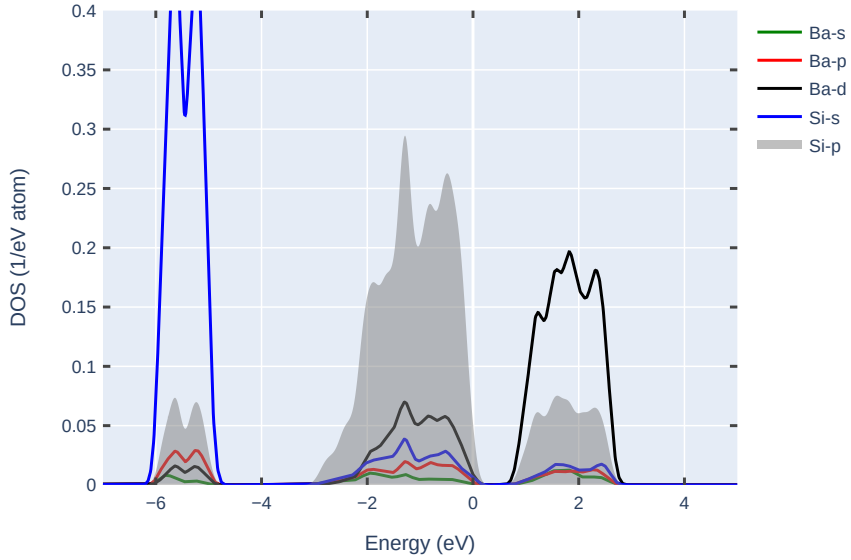
DOS (1/eV atom)
Energy (eV)
Ba-s
Ba-p
Ba-d
Si-s
Si-p

(a) L2

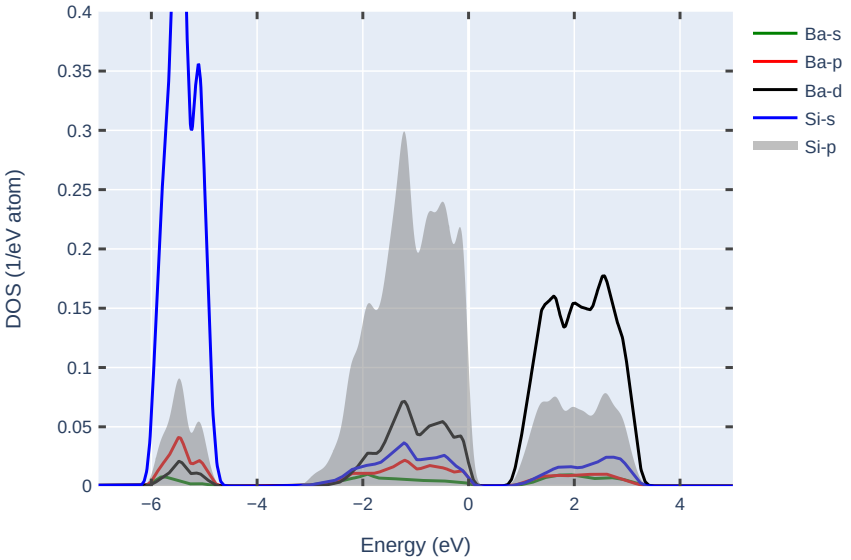
DOS (1/eV atom)
Energy (eV)
Ba-s
Ba-p
Ba-d
Si-s
Si-p

(b) L3

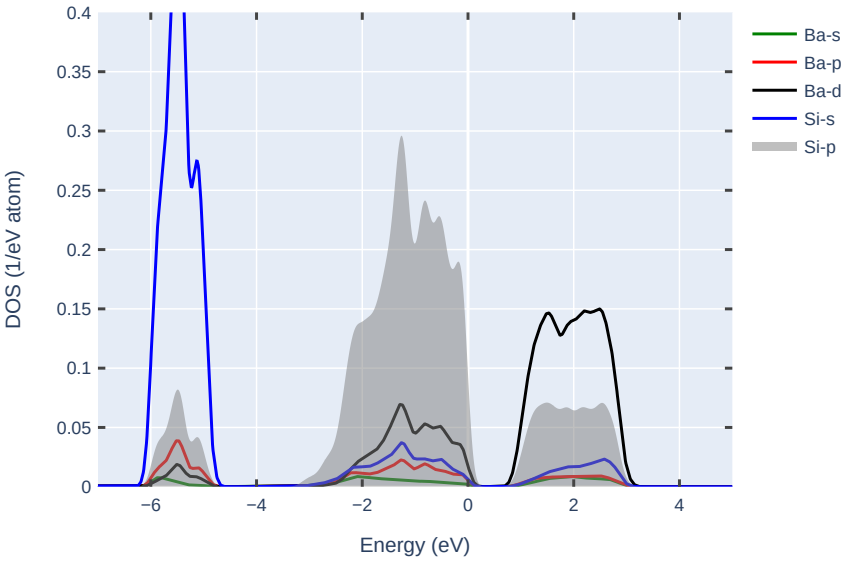

(c) L4

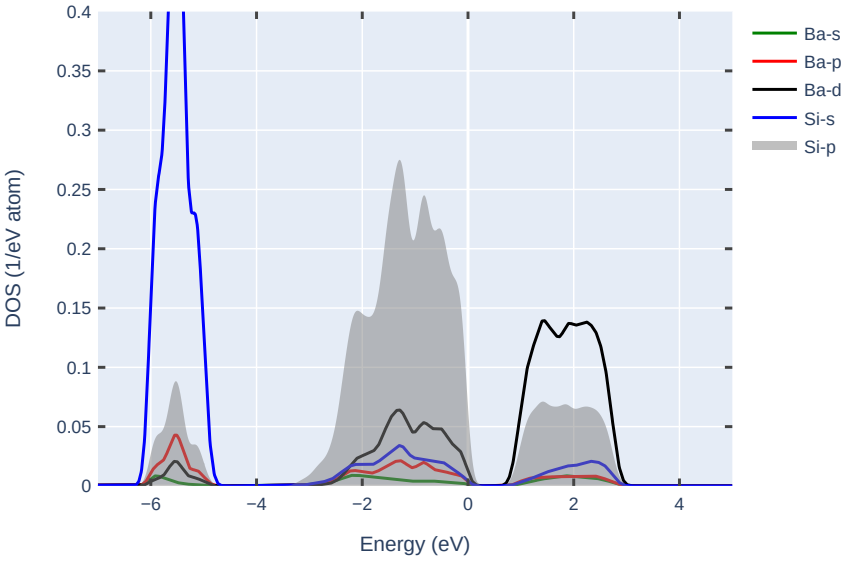

(d) L5

Figure 6.11: Atomically resolved DOS of a) L2, b) L3, c) L4 and d) L5. The zero of the absolute energy is set to the VBM.

6.3.3 Optical Properties

As we mentioned earlier, to study the optical properties of 2D materials, we have to compensate for the vacuum, and to do that we need the thickness of the layered structures. It turns out that the thickness of the monolayer can be estimated by using the interlayer spacing of the material, which was discussed in the paper of Hess [63], where they studied the thickness of different 2D structures. Graphite is the perfect example of this, where it has an interlayer spacing of 3.41 Å, and the thickness of a single graphene layer was found to be 3.4 Å. Therefore, by calculating the interlayer distance of $BaSi_2$, we can estimate the thickness of a single 2D-layer, and utilize this to estimate the thickness of the multilayer system as the thickness of the monolayer times the number of layers.

To make sure that the calculation of the interlayer distance of $BaSi_2$ is correct, a verification was needed. Therefore, we have calculated the interlayer spacing of graphite using the rev-vdW-DF2 functional, which is shown in Figure 6.12.

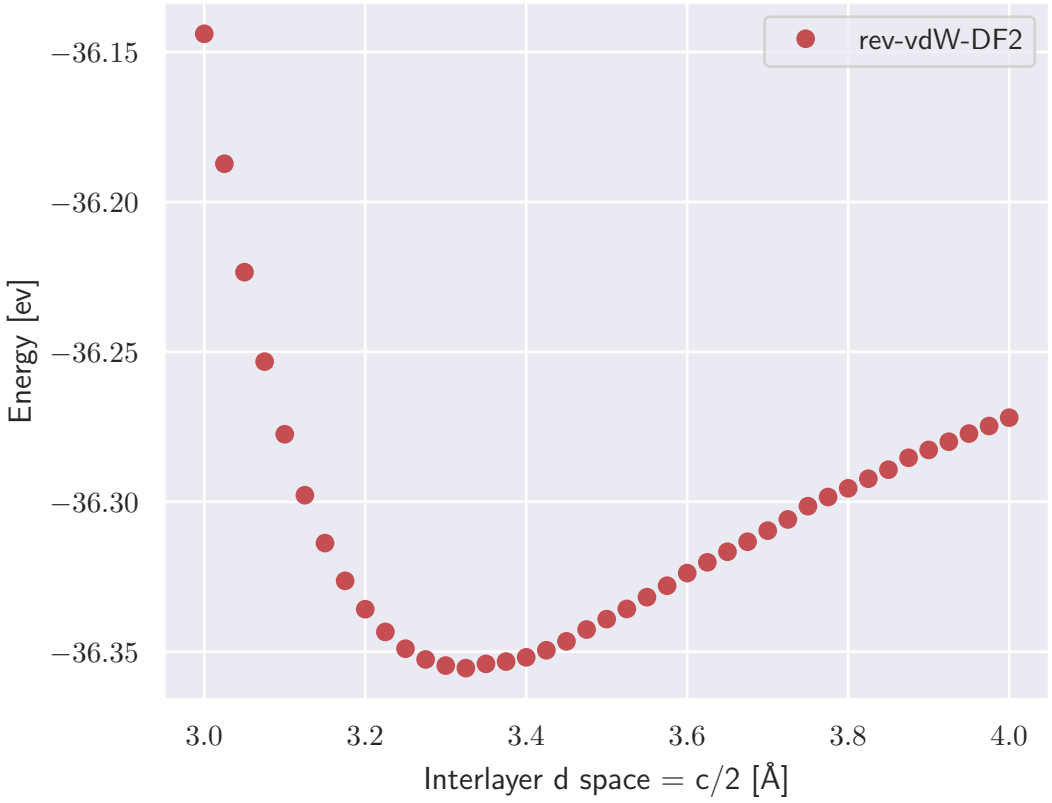

Figure 6.12: Interlayer spacing of graphite, where the total energy of the system is plotted as a function of the interlayer distance.

The interlayer distance was calculated to be 3.325 Å, which is relative close to the experimentally measured value of 3.4 Å of the thickness of graphene. After verifying that the rev-vdW-DF2 functional is somewhat able to calculate the interlayer distance correctly for graphite, we calculated the interlayer distance of $BaSi_2$, and the result is shown in Figure 6.13. The interlayer distance for $BaSi_2$ was calculated to be 4.45 Å, which means our estimate for the thickness of the monolayer is 4.45 Å. With the thickness of the layers known, we could finally calculate the dielectric functions and absorption coefficient of the 2D-layers.

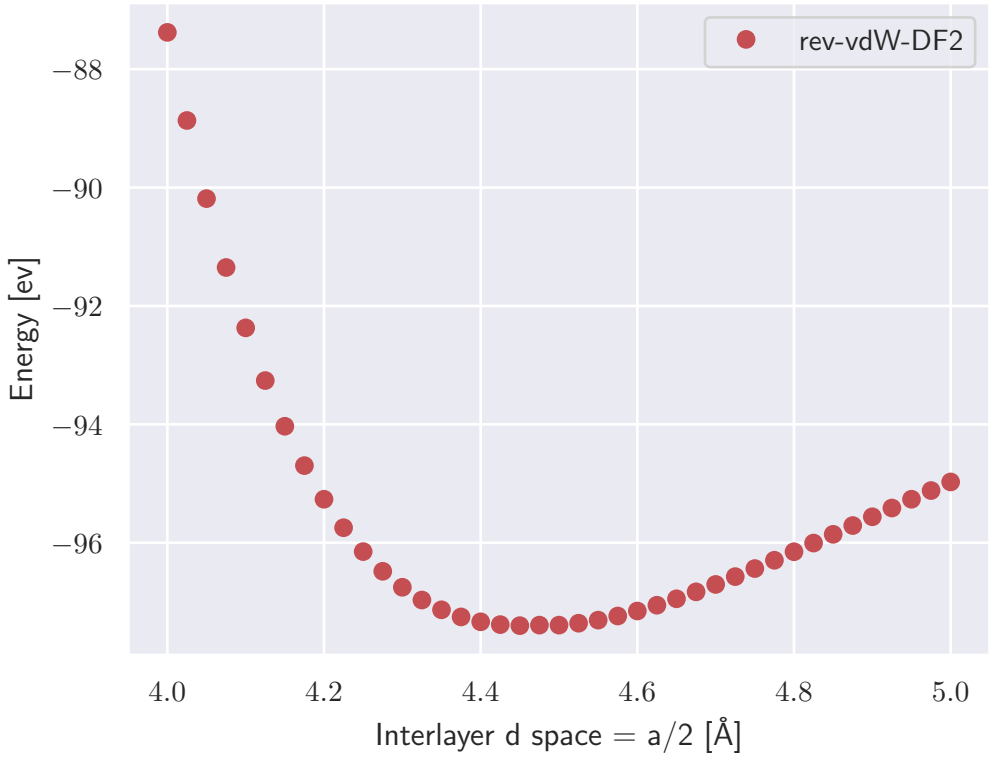

Figure 6.13: Interlayer spacing of $BaSi_2$, where the total energy of the system is plotted as a function of the interlayer distance.

The real and imaginary dielectric functions was only calculated for layers from L2 up to L5. The results are found in Figure 6.14. As observed for the bulk, we observe that both the real and imaginary dielectric function exhibits anisotropic behaviour, and that the dielectric response spectra seems to be similar to the bulk. However, there are some differences between the dielectric spectra between the layered structures. The imaginary part ϵ_2 of L2 seems to have sharper peaks than the other layered structures, but the peaks seems to damped when the number of layers increase in the 2D structures.

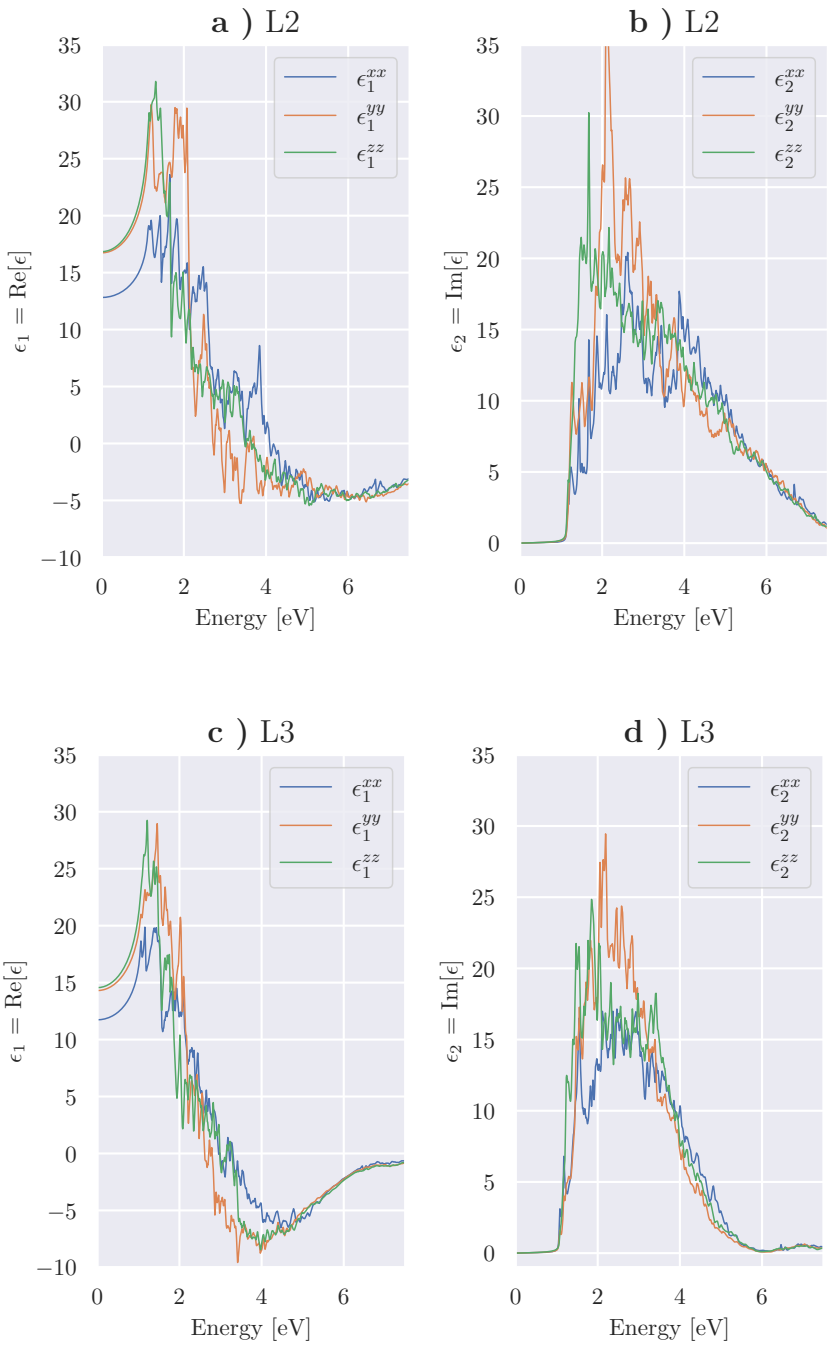
a) L2
b) L2
c) L3
d) L3
$\epsilon_1 = \mathrm{Re}[\epsilon]$
$\epsilon_2 = \mathrm{Im}[\epsilon]$
Energy [eV]
ϵ_1^{xx}
ϵ_1^{yy}
ϵ_1^{zz}
ϵ_2^{xx}
ϵ_2^{yy}
ϵ_2^{zz}

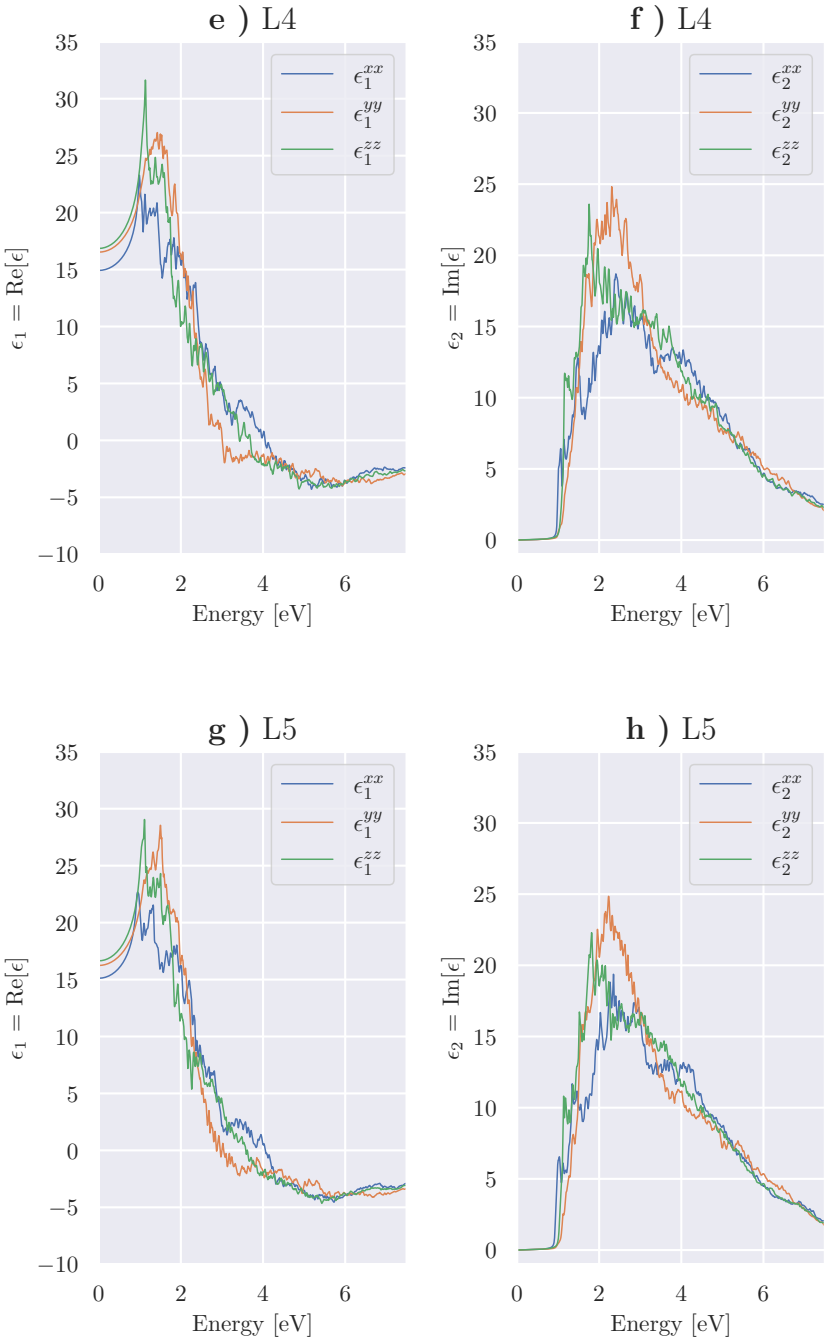

Figure 6.14: The components of the real and imaginary dielectric function, plotted against the photon energy across the xx, yy, and zz tensors, for different 2D layered structure of $BaSi_2$. The left-hand panels show the real part ϵ_1 and the right-hand panels show the imaginary part ϵ_2 of the dielectric function.

From the dielectric functions, we calculated the absorption coefficient in the same manner as we did for the bulk. The average absorption coefficient was calculated, and is shown in Figure 6.15.

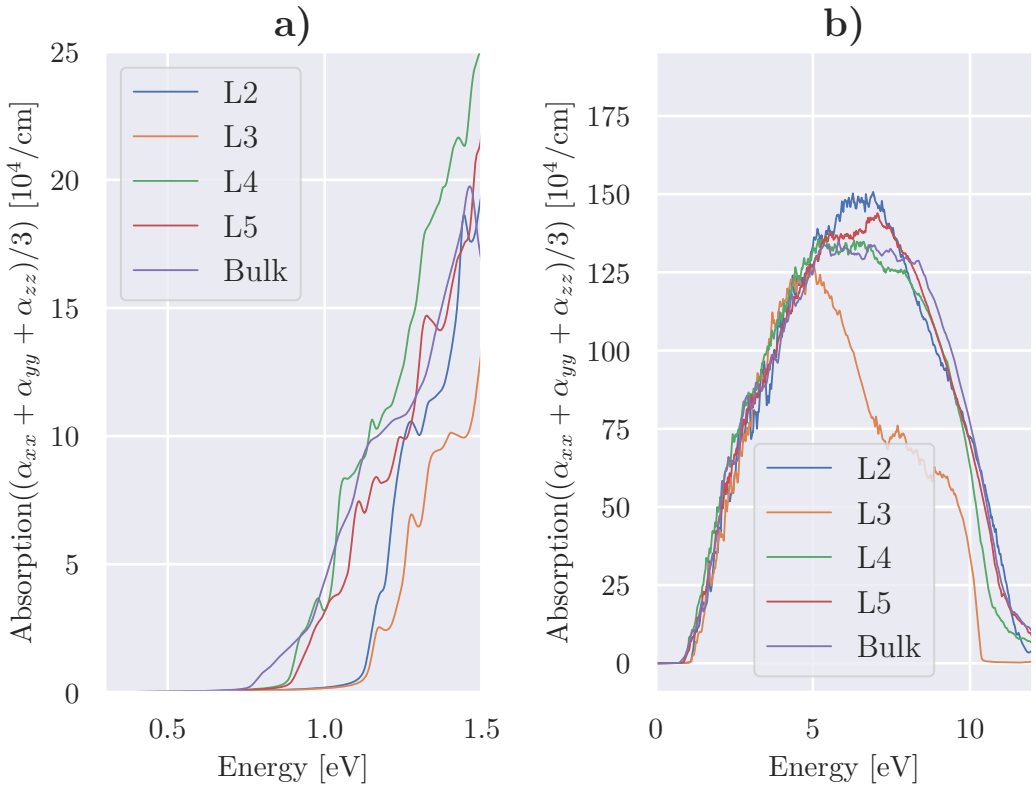

Figure 6.15: The aborption coefficient $\alpha(\omega)$ of 2D-layers from L2-L5 and the bulk, plotted against the photon energies, where a) shows the onset absorption region and b) shows the absorption over a broader region.

From Figure 6.15 a) we observe that the onset of the absorption is different for each 2D-layer, which is due to the difference in the optical band gap energy for the structures. The bulk which was measured to have the lowest optical band gap energy among the structures, have its onset first, while L2 and L3 structures have the onset at the highest photon energies. When we look at the absorption spectra over a broader region in 6.15 b), we see that all of the layered structures have an absorption spectra similar to the bulk, but the L3 structure does stand out from the rest of the layered structures, where the shape of it's absorption spectra is a little different. However, all of the structures have an absorption in the range of 1-10 eV, and both the visible and ultraviolet light lies in this energy level, which might make the 2D-layered structure of $BaSi_2$ a possible candidate in photo-detection and solar cell applications. The layered structures also seem to have a large absorption coefficient, similar to the bulk at $\sim 10^6$ cm^{-1}, which only makes the 2D layered structures more applicable within solar cells.

However, the optical calculations for the layered systems were obtained using the approximation we discussed earlier, with using the thickness of the layers. This estimation does introduce an uncertainty and possibly errors, which is difficult to quantisize. Therefore, the results discussed here in this subsection needs to be carefully considered, and needs to be compared with other similar results.

Chapter 7

Conclusion

In this chapter, the findings of this work will be summarized and further work to get an even deeper understanding of the two-dimensional structure of $BaSi_2$ is suggested.

7.1 Summary

In this work the structural, electronic and optical properties of the two-dimensional structure of $BaSi_2$ was studied, using DFT. To fully understand the two-dimensional structure of $BaSi_2$, calculations for the bulk structure of $BaSi_2$ and $BaGe_2$ were carried out to ensure the right choice of functional for the two-dimensional study was done.

The structural calculations for the bulk structures showed that the rev-vdW-DF2, vdW-opt88 and HSE06 functional were the best performing functionals when compared to the experimental results. Focusing on the rev-vdW-DF2 and vdW-opt88 functionals, there was no clear indication of which functional performed the best. Therefore, we followed the discussion found in Tran et al. [47], where they did an extensive study of different vdW-functionals, and concluded that the rev-vdW-DF2 functional was the best choice.

The calculations regarding the electronic properties for the bulk structures showed that the rev-vdW-DF2 functional was able to capture the features of the band structure and atomically resolved density of states. For example, it did show both $BaSi_2$ and $BaGe_2$ are semiconductors with an indirect band gap, and also the contributions from the atomic orbitals were similar to results by Kumar et al. [12]. However, the rev-vdW-DF2 functional was not able to fully capture all the electronic properties, such as the band gap energy. In particular, it underestimated the fundamental band gap energy and optical band gap energy by a large margin, compared to the HSE06 functional which was much closer to the experimental values.

The optical calculations obtained by the rev-vdW-DF2 functional showed the dielectric function and absorption coefficient to be anistropic, and the values for the dielectric function and absorption coefficient were similar to results published by Kumar et al. [12], but there was a difference in the onset of absorption between our results and Kumar et al. [12], which was due to the underestimation of the optical band gap. Furthermore, the rev-vdW-DF2 was also able to confirm the experimental results of [57, 58, 59, 60], regarding the absorption coefficient being larger than 10^4 cm^{-1} for $BaSi_2$.

In the case of the single layer 2D-material of $BaSi_2$, things were not as simple. The monolayer was relaxed using two different methods, namely quasi-Newton and conjugate gradient. The two methods gave different results, were in the case of the conjugate gradient method, the monolayer was reconstructured, whereas the quasi-Newton method was able to relax the system with no reconstruction. Even though the conjugate gradient method reconstructured the monolayer, it did

have the lowest energy compared with the structure of the quasi-Newton method, which means that the quasi-Newton method found a local minima when relaxing the structure and obtained a metastable structure. The conjugate gradient method does suggest that the monolayer of $BaSi_2$ is unstable, which was confirmed by the findings in Choudhary [61], and the same study also indicated that the metastable monolayer was unstable due to the high exfoliation energy of the structure.

Next we looked in to the multilayered 2D structure of $BaSi_2$. First the structural properties and energies of the mulit-layered 2D structures were calculated using the rev-vdW-DF2 functional and compared with the bulk's values. The results showed a clear trend, where the increase in the thickness of the layered 2D structures caused the properties of the 2D system to converge towards the bulk's properties. The energy calculations showed that the multilayered 2D structures become more stabile as the number of layers in the structure increased.

Then the electronic properties of the 2D multilayered structures was studied. It was found that all the layered structures were semiconducting materials with an indirect band gap, just as the bulk structure. However, there was a difference, and that occurred for the layered structures L2-L4, where the location of the VBM and/or CBM was different from the bulk, but after a certain layer thickness (L5), the location of the VBM and CBM became the same as the bulk. Another interesting thing about the electronic properties was the band gap energy of the 2D layered structures. All of the layered structures had a higher band gap energy than the bulk, but as the number of layers increased in the structure, the band gap energy seemed to converge towards the bulk's value, which is the same trend observed of the structural properties. Unfortunately, the rev-vdW-DF2 functional underestimates the band gap energies, and therefore the band gap energies for L2-L5 was also calculated using the hybrid functional. The results showed the same trend of the band gap energy as the calculation done by rev-vdW-DF2 functional, where the band gap energy was dependent on the layer thickness. Moreover, the band gap energies for L2-L5 was in the range of $1.0-1.5$ eV, which is a suitable band gap range according to the Shockley-Queisser criterion [56].

The optical calculations for the multilayered were next investigated, but due to the vacuum introduced to the 2D-structures an approximation was made to take this into account. The approximation utilized the thickness of the layers, which was determined through the interlayer distance of the bulk. The thickness of the monolayer was found to be 4.45 Å, and to calculate the thickness of the multilayered systems, the thickness of the monolayer was multiplied with the number of layers found in the 2D-layered system. After finding the thickness of the layered structures, the dielectric function and absorption coefficient of L2-L5 was shown. The dielectric function was observed to be anisotropic similar to the bulk, and as the thickness of the layers increased, the dielectric function looked more similar to the bulk. The absorption coefficient for the 2D layered structures also exhibited anisotropic behaviour, similar to the bulk. The absorption coefficient for all the 2D-layered structures possessed a large absorption coefficient ($\sim 10^6$ cm^{-1}), which makes the structures more interesting as possible candidates for solar cell materials.

7.2 Future Work

The work presented in this thesis has revealed new insights into the two-dimensional capabilities of $BaSi_2$. Although several questions have been answered, additional investigations and improvements would enhance our understanding further. In particular the stability issue for the 2D-monolayer of $BaSi_2$, which could be studied further using phonon calculations to verify the results of unstability. The electronic properties of the 2D layered systems could also have been studied further, where a spin orbit coupling calculation could have brought new characteristics of the material to the open. In addition, the band gap energy of the thicker 2D-layers of $BaSi_2$ could also be calculated using the hybrid functional, to obtain better estimates for the band gap energies. To get a better description of the optical properties of the 2D layered structures, the static dielectric function could be calculated. Also, when it comes to the optical calculations for the 2D layered systems, other methods that takes the vacuum into account should be tested, to verify the results of our calculations.

Bibliography

[1] IEA (2020). Electricity information: Overview, 2020. URL https://www.iea.org/reports/electricity-information-overview.

[2] Major-Ex G. Climate, Sustainablility, Technology how to solve global warming, 2018. URL https://sites.middlebury.edu/climatechange/2018/05/02/how-to-solve-global-warming/.

[3] Stephen Cass. Solar power will make a difference–eventually, 2009. URL https://www.technologyreview.com/2009/08/18/210913/solar-power-will-make-a-difference-eventually/.

[4] Dricus De Rooij. Solar cell guide, part 2 - thin film (cdte, cigs) solar cells, 2012. URL https://sinovoltaics.com/solar-cells/solar-cell-guide-part-2-thin-film-cdte-cigs-solar-cells/.

[5] Michael Berger. Graphene and other 2d materials for advanced solar cells, 2019. URL https://www.nanowerk.com/spotlight/spotid=51821.php.

[6] Zahra Rafiei-Sarmazdeh, Seyed Morteza Zahedi-Dizaji, and Aniseh Kafi Kang. Two-dimensional nanomaterials. In Sadia Ameen, M. Shaheer Akhtar, and Hyung-Shik Shin, editors, *Nanostructures*, chapter 3. IntechOpen, Rijeka, 2020. doi: 10.5772/intechopen.85263. URL https://doi.org/10.5772/intechopen.85263.

[7] Material Science Engineering. Material structure, 2006. URL https://depts.washington.edu/matseed/ces_guide/material_structure.htm.

[8] Khan Academy. Intramolecular and intermolecular forces. URL https://www.khanacademy.org/science/class-11-chemistry-india/xfbb6cb8fc2bd00c8:in-in-states-of-matter/xfbb6cb8fc2bd00c8:in-in-intermolecular-forces/a/intramolecular-and-intermolecular-forces.

[9] Janice A Steckel David S, Sholl. *Density Functional Theory - A Practical Introduction*. John Wiley & Sons, Inc, 2009.

[10] Band theory of metals and insulators., 2021. URL https://chem.libretexts.org/@go/page/33310.

[11] K. Momma and F. Izumi. Vesta 3 for three-dimensional visualization of crystal, volumetric and morphology data. *J. Appl. Cryst.*, 44:1272–1276, 2011. doi: 10.1107/S0021889811038970. URL https://doi.org/10.1107/S0021889811038970.

[12] Mukesh Kumar, Naoto Umezawa, and Motoharu Imai. (sr,ba)(si,ge)2 for thin-film solar-cell applications: First-principles study. *Journal of Applied Physics*, 115(20):203718, 2014. doi: 10.1063/1.4880662. URL https://doi.org/10.1063/1.4880662.

[13] Tianguo Deng, Takuma Sato, Zhihao Xu, Ryota Takabe, Suguru Yachi, Yudai Yamashita, Kaoru Toko, and Takashi Suemasu. p-BaSi2/n-si heterojunction solar cells on si(001) with

conversion efficiency approaching 10%: comparison with si(111). *Applied Physics Express*, 11(6):062301, may 2018. doi: 10.7567/apex.11.062301. URL https://doi.org/10.7567/apex.11.062301.

[14] M. Ajmal Khan, K. O. Hara, W. Du, M. Baba, K. Nakamura, M. Suzuno, K. Toko, N. Usami, and T. Suemasu. In-situ heavily p-type doping of over 1020cm3 in semiconducting basi2 thin films for solar cells applications. *Applied Physics Letters*, 102(11):112107, 2013. doi: 10.1063/1.4796142. URL https://doi.org/10.1063/1.4796142.

[15] M. Ajmal Khan, K. Nakamura, W. Du, K. Toko, N. Usami, and T. Suemasu. Precipitation control and activation enhancement in boron-doped p+-basi2 films grown by molecular beam epitaxy. *Applied Physics Letters*, 104(25):252104, 2014. doi: 10.1063/1.4885553. URL https://doi.org/10.1063/1.4885553.

[16] David J. Griffiths. *Introduction to Quantum Mechanics*. Pearson Education International, second edition, 2005.

[17] Persson C. *Quantum Mechanical Modeling of Nano-Materials — Lecture Notes*. 2013.

[18] P. Hohenberg and W. Kohn. Inhomogenous electron gas. *Phys. Rev.*, 136, 1964. doi: 10.1103/PhysRev.136.B864. URL https://doi.org/10.1103/PhysRev.136.B864.

[19] W. Kohn and L. J. Sham. Self-consistent equations including exchange and correlation effects. *Phys. Rev.*, 140, 1965. doi: 10.1103/PhysRev.136.B864. URL https://doi.org/10.1103/PhysRev.140.A1133.

[20] Clark S J. Local density approximation, 2003. URL http://cmt.dur.ac.uk/sjc/thesis_dlc/node29.html.

[21] Jeremy P. Allen and Graeme W. Watson. Occupation matrix control of d- and f-electron localisations using dft + u. *Phys. Chem. Chem. Phys.*, 16:21016–21031, 2014. doi: 10.1039/C4CP01083C. URL http://dx.doi.org/10.1039/C4CP01083C.

[22] John P. Perdew, J. A. Chevary, S. H. Vosko, Koblar A. Jackson, Mark R. Pederson, D. J. Singh, and Carlos Fiolhais. Atoms, molecules, solids, and surfaces: Applications of the generalized gradient approximation for exchange and correlation. *Phys. Rev. B*, 46:6671–6687, Sep 1992. doi: 10.1103/PhysRevB.46.6671. URL https://link.aps.org/doi/10.1103/PhysRevB.46.6671.

[23] John P. Perdew, J. A. Chevary, S. H. Vosko, Koblar A. Jackson, Mark R. Pederson, D. J. Singh, and Carlos Fiolhais. Erratum: Atoms, molecules, solids, and surfaces: Applications of the generalized gradient approximation for exchange and correlation. *Phys. Rev. B*, 48:4978–4978, Aug 1993. doi: 10.1103/PhysRevB.48.4978.2. URL https://link.aps.org/doi/10.1103/PhysRevB.48.4978.2.

[24] John P. Perdew, Kieron Burke, and Matthias Ernzerhof. Generalized gradient approximation made simple. *Phys. Rev. Lett.*, 77:3865–3868, Oct 1996. doi: 10.1103/PhysRevLett.77.3865. URL https://link.aps.org/doi/10.1103/PhysRevLett.77.3865.

[25] John P. Perdew, Kieron Burke, and Matthias Ernzerhof. Generalized gradient approximation made simple [phys. rev. lett. 77, 3865 (1996)]. *Phys. Rev. Lett.*, 78:1396–1396, Feb 1997. doi: 10.1103/PhysRevLett.78.1396. URL https://link.aps.org/doi/10.1103/PhysRevLett.78.1396.

[26] Jochen Heyd, Gustavo E. Scuseria, and Matthias Ernzerhof. Hybrid functionals based on a screened coulomb potential. *The Journal of Chemical Physics*, 118(18):8207–8215, 2003. doi: 10.1063/1.1564060. URL https://doi.org/10.1063/1.1564060.

[27] P. E. Blöchl. Projector augmented-wave method. *Phys. Rev. B*, 50:17953–17979, Dec 1994. doi: 10.1103/PhysRevB.50.17953. URL https://link.aps.org/doi/10.1103/PhysRevB.50.17953.

[28] Hendrik J. Monkhorst and James D. Pack. Special points for brillouin-zone integrations. *Phys. Rev. B*, 13:5188–5192, Jun 1976. doi: 10.1103/PhysRevB.13.5188. URL https://link.aps.org/doi/10.1103/PhysRevB.13.5188.

[29] G. Kresse and J. Hafner. Ab initio molecular dynamics for liquid metals. *Phys. Rev. B*, 47:558–561, Jan 1993. doi: 10.1103/PhysRevB.47.558. URL https://link.aps.org/doi/10.1103/PhysRevB.47.558.

[30] G. Kresse and J. Hafner. Ab initio molecular-dynamics simulation of the liquid-metal–amorphous-semiconductor transition in germanium. *Phys. Rev. B*, 49:14251–14269, May 1994. doi: 10.1103/PhysRevB.49.14251. URL https://link.aps.org/doi/10.1103/PhysRevB.49.14251.

[31] G. Kresse and J. Furthmüller. Efficiency of ab-initio total energy calculations for metals and semiconductors using a plane-wave basis set. *Computational Materials Science*, 6(1):15–50, 1996. ISSN 0927-0256. doi: https://doi.org/10.1016/0927-0256(96)00008-0. URL https://www.sciencedirect.com/science/article/pii/0927025696000080.

[32] G. Kresse and J. Furthmüller. Efficient iterative schemes for ab initio total-energy calculations using a plane-wave basis set. *Phys. Rev. B*, 54:11169–11186, Oct 1996. doi: 10.1103/PhysRevB.54.11169. URL https://link.aps.org/doi/10.1103/PhysRevB.54.11169.

[33] G. Kresse and D. Joubert. From ultrasoft pseudopotentials to the projector augmented-wave method. *Phys. Rev. B*, 59:1758–1775, Jan 1999. doi: 10.1103/PhysRevB.59.1758. URL https://link.aps.org/doi/10.1103/PhysRevB.59.1758.

[34] John P. Perdew, Kieron Burke, and Matthias Ernzerhof. Generalized gradient approximation made simple. *Phys. Rev. Lett.*, 77:3865–3868, Oct 1996. doi: 10.1103/PhysRevLett.77.3865. URL https://link.aps.org/doi/10.1103/PhysRevLett.77.3865.

[35] John P. Perdew, Kieron Burke, and Matthias Ernzerhof. Generalized gradient approximation made simple [phys. rev. lett. 77, 3865 (1996)]. *Phys. Rev. Lett.*, 78:1396–1396, Feb 1997. doi: 10.1103/PhysRevLett.78.1396. URL https://link.aps.org/doi/10.1103/PhysRevLett.78.1396.

[36] Stefan Grimme, Jens Antony, Stephan Ehrlich, and Helge Krieg. A consistent and accurate ab initio parametrization of density functional dispersion correction (dft-d) for the 94 elements h-pu. *The Journal of Chemical Physics*, 132(15):154104, 2010. doi: 10.1063/1.3382344. URL https://doi.org/10.1063/1.3382344.

[37] Jiří Klimeš, David R Bowler, and Angelos Michaelides. Chemical accuracy for the van der waals density functional. *Journal of Physics: Condensed Matter*, 22(2):022201, dec 2009. doi: 10.1088/0953-8984/22/2/022201. URL https://doi.org/10.1088/0953-8984/22/2/022201.

[38] Ji ří Klimeš, David R. Bowler, and Angelos Michaelides. Van der waals density functionals applied to solids. *Phys. Rev. B*, 83:195131, May 2011. doi: 10.1103/PhysRevB.83.195131. URL https://link.aps.org/doi/10.1103/PhysRevB.83.195131.

[39] Ikutaro Hamada. van der waals density functional made accurate. *Phys. Rev. B*, 89:121103, Mar 2014. doi: 10.1103/PhysRevB.89.121103. URL https://link.aps.org/doi/10.1103/PhysRevB.89.121103.

[40] Aliaksandr V. Krukau, Oleg A. Vydrov, Artur F. Izmaylov, and Gustavo E. Scuseria. Influence of the exchange screening parameter on the performance of screened hybrid functionals. *The Journal of Chemical Physics*, 125(22):224106, 2006. doi: 10.1063/1.2404663. URL https://doi.org/10.1063/1.2404663.

[41] Wahyu Setyawan and Stefano Curtarolo. High-throughput electronic band structure calculations: Challenges and tools. *Computational Materials Science*, 49(2):299–312, 2010. ISSN 0927-0256. doi: https://doi.org/10.1016/j.commatsci.2010.05.010. URL https://www.sciencedirect.com/science/article/pii/S0927025610002697.

[42] R. Chen, S. Zamulko, Dan Huang, and C. Persson. Chapter 5 theoretical analyses of copper-based solar cell materials for the next generation of photovoltaics. In *Solar Energy Capture Materials*, pages 193–240. The Royal Society of Chemistry, 2019. ISBN 978-1-78801-107-5. doi: 10.1039/9781788013512-00193. URL http://dx.doi.org/10.1039/9781788013512-00193.

[43] A. Betz, Herbert Schäfer, Armin Weiss, and R. Wulf. Notizen: Zur kenntnis der digermanide des strontiums und bariums, srge2 und bage2. *Zeitschrift für Naturforschung B*, 23(6):878–878, 1968. doi: doi:10.1515/znb-1968-0624. URL https://doi.org/10.1515/znb-1968-0624.

[44] Motoharu Imai. Energy gap of alkaline-earth-metal digermanides srge2 and bage2. *physica status solidi c*, 10(12):1728–1731, 2013. doi: https://doi.org/10.1002/pssc.201300375. URL https://onlinelibrary.wiley.com/doi/abs/10.1002/pssc.201300375.

[45] Jürgen Evers. Transformation of three-connected silicon in basi2. *Journal of Solid State Chemistry*, 32(1):77–86, 1980. ISSN 0022-4596. doi: https://doi.org/10.1016/0022-4596(80)90270-4. URL https://www.sciencedirect.com/science/article/pii/0022459680902704.

[46] Herbert Schäfer, K. H. Janzon, and Armin Weiss. Basi2, a phase with discrete si4 tetrahedra. *Angewandte Chemie International Edition in English*, 2(7):393–394, 1963. doi: https://doi.org/10.1002/anie.196303932. URL https://onlinelibrary.wiley.com/doi/abs/10.1002/anie.196303932.

[47] Fabien Tran, Leila Kalantari, Boubacar Traoré, Xavier Rocquefelte, and Peter Blaha. Nonlocal van der waals functionals for solids: Choosing an appropriate one. *Phys. Rev. Materials*, 3: 063602, Jun 2019. doi: 10.1103/PhysRevMaterials.3.063602. URL https://link.aps.org/doi/10.1103/PhysRevMaterials.3.063602.

[48] Motoharu Imai. Energy gap of alkaline-earth-metal digermanides srge 2 and bage 2. *Physica status solidi.*, 10(12):1728–1731, 2013. ISSN 1862-6351.

[49] J. Evers and A. Weiss. Electrical properties of alkaline earth disilicides and digermanides. *Materials Research Bulletin*, 9(5):549–553, 1974. ISSN 0025-5408. doi: https://doi.org/10.1016/0025-5408(74)90124-X. URL https://www.sciencedirect.com/science/article/pii/002554087490124X.

[50] Tomoyuki Nakamura, Takashi Suemasu, Ken-ichiro Takakura, Fumio Hasegawa, Akihiro Wakahara, and Motoharu Imai. Investigation of the energy band structure of orthorhombic basi2 by optical and electrical measurements and theoretical calculations. *Applied physics letters*, 81(6):1032–1034, 2002. ISSN 0003-6951.

[51] LI Ivanenko, VL Shaposhnikov, AB Filonov, AV Krivosheeva, VE Borisenko, DB Migas, L Miglio, G Behr, and J Schumann. Electronic properties of semiconducting silicides: fundamentals and recent predictions. *Thin solid films*, 461(1):141–147, 2004. ISSN 0040-6090.

[52] Yuya Inomata, Tomoyuki Nakamura, Takashi Suemasu, and Fumio Hasegawa. Epitaxial growth of semiconducting basi 2 thin films on si(111) substrates by reactive deposition epitaxy. *Japanese journal of applied physics*, 43(7R):4155–4156, 2004. ISSN 0021-4922.

[53] K Morita, Y Inomata, and T Suemasu. Optical and electrical properties of semiconducting basi2 thin films on si substrates grown by molecular beam epitaxy. *Thin solid films*, 508(1-2): 363–366, 2006. ISSN 0040-6090.

[54] Yuta Matsumoto, Dai Tsukada, Ryo Sasaki, Mitsutomo Takeishi, and Takashi Suemasu. Photoresponse properties of semiconducting basi 2 epitaxial films grown on si(111) substrates by molecular beam epitaxy. *Applied physics express.*, 2(2):021101, 2009. ISSN 1882-0778.

[55] Takanobu Saito, Yuta Matsumoto, Ryo Sasaki, Michitoshi Takeishi, and Takashi Suemasu. Impact of thin island-like basi 2 template on the formation of n + -basi 2 /p + -si tunnel junction on si(111) surface by molecular beam epitaxy. *Japanese journal of applied physics*, 49(6R):068001, 2010. ISSN 0021-4922.

[56] William Shockley and Hans J. Queisser. Detailed balance limit of efficiency of p-n junction solar cells. *Journal of Applied Physics*, 32(3):510–519, 1961. doi: 10.1063/1.1736034. URL https://doi.org/10.1063/1.1736034.

[57] Yuya Inomata, Tomoyuki Nakamura, Takashi Suemasu, and Fumio Hasegawa. Epitaxial growth of semiconducting BaSi2thin films on si(111) substrates by reactive deposition epitaxy. *Japanese Journal of Applied Physics*, 43(7A):4155–4156, jul 2004. doi: 10.1143/jjap.43.4155. URL https://doi.org/10.1143/jjap.43.4155.

[58] Yuya Inomata, Tomoyuki Nakamura, Takashi Suemasu, and Fumio Hasegawa. Epitaxial growth of semiconducting BaSi2films on si(111) substrates by molecular beam epitaxy. *Japanese Journal of Applied Physics*, 43(No. 4A):L478–L481, mar 2004. doi: 10.1143/jjap.43.l478. URL https://doi.org/10.1143/jjap.43.l478.

[59] Yuta Matsumoto, Dai Tsukada, Ryo Sasaki, Mitsutomo Takeishi, and Takashi Suemasu. Photoresponse properties of semiconducting BaSi2epitaxial films grown on si(111) substrates by molecular beam epitaxy. *Applied Physics Express*, 2:021101, feb 2009. doi: 10.1143/apex.2.021101. URL https://doi.org/10.1143/apex.2.021101.

[60] Takanobu Saito, Yuta Matsumoto, Ryo Sasaki, Michitoshi Takeishi, and Takashi Suemasu. Impact of thin island-like BaSi2template on the formation of n-BaSi2/p-si tunnel junction on si(111) surface by molecular beam epitaxy. *Japanese Journal of Applied Physics*, 49(6):068001, jun 2010. doi: 10.1143/jjap.49.068001. URL https://doi.org/10.1143/jjap.49.068001.

[61] Kalish I. Beams R. Choudhary, K. High-throughput identification and characterization of two-dimensional materials using density functional theory. *Scientific Reports*, 7:5179, 2017. ISSN 2045-2322. doi: 10.1038/s41598-017-05402-0. URL https://doi.org/10.1038/s41598-017-05402-0.

[62] Shan Gao Yonghong Zeng Fanxu Meng Zhinan Guo Han Zhang David K. Sang, Bo Wen. Electronic and optical properties of two-dimensional tellurene: From first-principles calculations. *Nanomaterials (Basel, Switzerland)*, 9, 2019. ISSN 2079-4991. doi: 10.3390/nano9081075. URL https://pubmed.ncbi.nlm.nih.gov/31357462.

[63] Peter Hess. Thickness of elemental and binary single atomic monolayers. *Nanoscale Horiz.*, 5:385–399, 2020. doi: 10.1039/C9NH00658C. URL http://dx.doi.org/10.1039/C9NH00658C.

Appendices

Appendix A

Density Functional Theory

A.1 Hohenberg-Kohn Theorems

A.1.1 The Hohenberg-Kohn theorem 1

Proof:
Assume that there exists two potentials $V_{ext}^{(1)}(\boldsymbol{r})$ and $V_{ext}^{(2)}(\boldsymbol{r})$ differing by more than a constant and giving rise to the same ground state density, $n(\boldsymbol{r})$. Obviously, $V_{ext}^{(1)}(\boldsymbol{r})$ and $V_{ext}^{(2)}(\boldsymbol{r})$ belong to distinct Hamiltonian's $\hat{H}_{ext}^{(1)}(\boldsymbol{r})$ and $\hat{H}_{ext}^{(2)}(\boldsymbol{r})$, which give rise to distinct wavefunctions $\Psi_{ext}^{(1)}(\boldsymbol{r})$ and $\Psi_{ext}^{(2)}(\boldsymbol{r})$. Because of the variational principle, no wavefunction can give an energy that is less than the energy of $\Psi_{ext}^{(1)}(\boldsymbol{r})$ for $\hat{H}_{ext}^{(1)}(\boldsymbol{r})$. That is:

$$
\begin{aligned}
E^{(1)} &= \langle \Psi^{(1)} | \hat{H}^{(1)} | \Psi^{(1)} \rangle < \langle \Psi^{(2)} | \hat{H}^{(1)} | \Psi^{(2)} \rangle \\
E^{(2)} &= \langle \Psi^{(2)} | \hat{H}^{(2)} | \Psi^{(2)} \rangle < \langle \Psi^{(1)} | \hat{H}^{(2)} | \Psi^{(1)} \rangle
\end{aligned}
$$

Assuming that the ground state is not degenerate, the inequality strictly holds. Because we have identical ground state densities for the two Hamiltonian's, we can rewrite the expectation value written above as:

$$
\begin{aligned}
E^{(1)} &= \langle \Psi^{(1)} | \hat{H}^{(1)} | \Psi^{(1)} \rangle = \langle \Psi^{(1)} | T + U_{ee} + U_{ext}^{(1)} | \Psi^{(1)} \rangle \\
&= \langle \Psi^{(1)} | T + U_{ee} | \Psi^{(1)} \rangle + \int \Psi^{*(1)}(\boldsymbol{r}) V_{ext}^{(1)} \Psi^{(1)}(\boldsymbol{r}) d\boldsymbol{r} \\
&= \langle \Psi^{(1)} | T + U_{ee} | \Psi^{(1)} \rangle + \int V_{ext}^{(1)} n(\boldsymbol{r}) d\boldsymbol{r} \\
&< \langle \Psi^{(2)} | \hat{H}^{(1)} | \Psi^{(2)} \rangle = \langle \Psi^{(2)} | T + U_{ee} + U_{ext}^{(1)} | \Psi^{(2)} \rangle \\
&= \langle \Psi^{(2)} | T + U_{ee} + U_{ext}^{(1)} + U_{ext}^{(2)} - U_{ext}^{(2)} | \Psi^{(2)} \rangle \\
&= \langle \Psi^{(2)} | T + U_{ee} + U_{ext}^{(2)} | \Psi^{(2)} \rangle + \int \left(V_{ext}^{(1)} - V_{ext}^{(2)} \right) n(\boldsymbol{r}) d\boldsymbol{r} \\
&= E^{(2)} + \int \left(V_{ext}^{(1)} - V_{ext}^{(2)} \right) n(\boldsymbol{r}) d\boldsymbol{r}
\end{aligned}
$$

Thus,

$$
E^{(1)} < E^{(2)} + \int \left(V_{ext}^{(1)} - V_{ext}^{(2)} \right) n(\boldsymbol{r}) d\boldsymbol{r}
$$

And similarly can be done for $E^{(2)}$:

$$E^{(2)} < E^{(1)} + \int \left(V_{ext}^{(2)} - V_{ext}^{(1)}\right) n(\boldsymbol{r}) d\boldsymbol{r}$$

And by adding the two equations we get:

$$E^{(1)} + E^{(2)} < E^{(2)} + E^{(1)} + \int \left(V_{ext}^{(1)} - V_{ext}^{(2)}\right) n(\boldsymbol{r}) d\boldsymbol{r} + \int \left(V_{ext}^{(2)} - V_{ext}^{(1)}\right) n(\boldsymbol{r}) d\boldsymbol{r}$$
$$E^{(1)} + E^{(2)} < E^{(2)} + E^{(1)}$$

This is a contradiction. Thus, the two external potentials cannot have the same ground-state density, and $V_{ext}(\boldsymbol{r})$ is a determined uniquely (except for a constant) by $n(\boldsymbol{r})$ [17].

A.1.2 The Hohenberg-Kohn theorem 2

Proof:
Since the external potential is uniquely determined by the density and since the potential in turn uniquely (except in degenerate situations) determines the ground state wavefunction, all the other observables of the system such as kinetic energy are uniquely determined. Then one may write the energy as a functional of the density.

$$\begin{aligned} E[n(\boldsymbol{r})] &= T[n(\boldsymbol{r})] + U_{ee}[n(\boldsymbol{r})] + U_{ext}[n(\boldsymbol{r})] \\ U_{ext}[n(\boldsymbol{r})] &= \int V_{ext} n(\boldsymbol{r}) d\boldsymbol{r} \\ F[n(\boldsymbol{r})] &= T[n(\boldsymbol{r})] + U_{ee}[n(\boldsymbol{r})] \\ E[n(\boldsymbol{r})] &= F[n(\boldsymbol{r})] + \int V_{ext} n(\boldsymbol{r}) d\boldsymbol{r} \end{aligned}$$

where $F[n]$ (is called the Hohenberg-Kohn functional) is a universal functional because the treatment of the kinetic and internal potential energies are the same for all systems. In the ground state, the energy is defined by the unique ground state density, $n_0(\boldsymbol{r})$

$$E_0 = E[n_0(\boldsymbol{r})] = \langle \Psi_0 | H | \Psi_0 \rangle$$

From the variational principle, a different density $n(\boldsymbol{r})$ will necessarily give a higher energy.

$$E_0 = E[n_0(\boldsymbol{r})] = \langle \Psi_0 | H | \Psi_0 \rangle < \langle \Psi | H | \Psi \rangle = E[n(\boldsymbol{r})]$$

It follows that minimizing with respect to $n(\boldsymbol{r})$ the total energy of the system written as a functional of $n(\boldsymbol{r})$, one finds the total energy of the ground state. The correct density that minimizes the energy is then the ground state density [17].

A.2 Derivation of the Kohn-Sham Equation

We start of with total energy as a functional of the density:

$$n(\boldsymbol{r}) = \sum_j |\psi_j(\boldsymbol{r})|^2$$

$$E[n] = T[n] + U_{ee}[n] + U_{ext}[n] = F[n] + \int V_{ext} n(\boldsymbol{r}) d\boldsymbol{r}$$

$T[n]$ is the kinetic energy of the many-electron system, and $U_{ee}[n]$ is the many-electron interaction energy. These functionals are unique, but unknown to date. Thus, even if we have the exact density we are not capable to calculate the exact energy.

Now we rewrite the equation above to:

$$\begin{aligned} E[n] &= T[n] + U_{ee}[n] + U_{ext}[n] + T_s[n] - T_s[n] + U_s[n] - U_s[n] \\ &= T_s[n] + U_s[n] + U_{ext}[n] + \Big(T[n] - T_s[n]\Big) + \Big(U_{ee}[n] - U_s[n]\Big) \end{aligned}$$

Where $\hat{T}_s[n]$ and $\hat{V}_s[n]$ are the kinetic energy and interaction energy which we can calculate. The remaining part will be defined as the exchange-correlation energy:

$$E_{xc}[n] = \Delta T + \Delta U = \Big(T[n] - T_s[n]\Big) + \Big(U_{ee}[n] - U_s[n]\Big)$$

This exchange-correlation energy contains the complex many-electron interaction, but it also contains a kinetic energy part (this fact is often forgotten when discussing the corrections). We have transformed the many-electron problem into an unknown exchange-correlation energy. $E_{xc}[n]$ is zero for a non-interacting system, but for a general system the energy has most likely very complicated expression. Our aim is to find a good approximation to this term.
The exchange-correlation energy can be regarded as the "left-over energy" that includes everything that we do not describe with T_s, U_s and U_{ext}.

The total energy is:

$$E[n] = T_s[n] + U_s[n] + U_{ext}[n] + E_{xs}[n]$$

Where

$$T_s[n] = \sum_j \int \psi_j^{s*} \frac{-\hbar^2 \nabla^2}{2m} \psi_j^s d\boldsymbol{r} \qquad : \text{kinetic energy in the Hartree approximation}$$

$$U_s[n] = \frac{1}{2} \int \int q^2 \frac{n(\mathbf{r}) n(\mathbf{r}')}{|\mathbf{r} - \mathbf{r}'|} d\mathbf{r} d\mathbf{r}' - \sum_{j=1,2} \frac{q^2 n_j(\mathbf{r}) n_{j'}(\mathbf{r}')}{|\mathbf{r} - \mathbf{r}'|} d\mathbf{r} d\mathbf{r}', : \text{electron interaction energy in the Hartree approx}$$

$$U_{ext}[n] = \int V_{ext}(\boldsymbol{r}) n(\boldsymbol{r}) d\boldsymbol{r} \qquad : \text{external potential (ex: electron-nucleus interaction energy)}$$

$$E_{xc}[n] = \Big(T[n] - T_s[n]\Big) + \Big(U_{ee}[n] - U_s[n]\Big) \qquad : \text{exchange-correlation energy (unknown)}$$

Note that one can use other approximations for $T_s[n]$ and $U_s[n]$ than Hartree. And the better approximations one uses the lower $E_{xc}[n]$ will get, since $T_s[n]$ and $U_s[n]$ will get closer and closer to the correct values.

The next step is to use the variational principle to find the ground-state energy, and to transform the many-electron system into many single-particle equations, just like Hartree approximation.

First one minimises the total energy with respect to each of the wave-functions with the constraint that the wave-functions shall be orthonormalized.

$$\frac{\partial}{\partial\psi_j^{s*}(\boldsymbol{r})}E[n] = \sum_{i,j}\lambda_{ij}\int\psi_i^{s*}(\boldsymbol{r}_i)\psi_j^s(\boldsymbol{r_j})d\boldsymbol{r}_i d\boldsymbol{r}_j$$

$$\frac{\partial}{\partial\psi_j^{s*}(\boldsymbol{r})}\Big(T_s[n]+U_s[n]+U_{ext}[n]+E_{xs}[n]\Big) = \lambda_j\psi_j^s(\boldsymbol{r}_j)$$

It is convenient to derivate the kinetic energy with respect to the wavefunction, whereas the two remaining functionals are easiest to derivate with respect to the density, utilizing the chain rules for functional derivatives:

$$\frac{\partial}{\partial\psi_j^{s*}(\boldsymbol{r})}T_s[n] + \frac{\partial}{\partial n(\boldsymbol{r})}\frac{\partial n(\boldsymbol{r})}{\partial\psi_j^{s*}(\boldsymbol{r})}\Big(U_s[n]+U_{ext}[n]+E_{xs}[n]\Big) = \lambda_j\psi_j^s(\boldsymbol{r}_j)$$

$$\frac{\partial n(\boldsymbol{r})}{\partial\psi_j^{s*}(\boldsymbol{r})} = \frac{\partial}{\partial\psi_j^{s*}(\boldsymbol{r})}\sum_j\psi_j^{s*}(\boldsymbol{r})\psi_j^s(\boldsymbol{r}) = \psi_j^s(\boldsymbol{r})$$

$$\frac{\partial}{\partial\psi_j^{s*}(\boldsymbol{r})}T_s[n] + \frac{\partial}{\partial n(\boldsymbol{r})}\Big(U_s[n]+U_{ext}[n]+E_{xs}[n]\Big)\psi_j^s(\boldsymbol{r}) = \lambda_j\psi_j^s(\boldsymbol{r}_j)$$

Where the derivatives are:

$$\frac{\partial}{\partial\psi_j^{s*}(\boldsymbol{r})}T_s[n] = \frac{\partial}{\partial\psi_j^{s*}(\boldsymbol{r})}\sum_j\int\psi_j^{s*}\frac{-\hbar^2\nabla^2}{2m}\psi_j^s d\boldsymbol{r} = \frac{-\hbar^2\nabla_j^2}{2m}\psi_j^s$$

$$\frac{\partial}{\partial n(\boldsymbol{r})}U_s[n] = \frac{\partial}{\partial n(\boldsymbol{r})}\frac{1}{2}\int\int q^2\frac{n(\mathbf{r})n(\mathbf{r}')}{|\mathbf{r}-\mathbf{r}'|}d\mathbf{r}d\mathbf{r}' - \sum_{j=1,2}\frac{q^2 n_j(\mathbf{r})n_{j'}(\mathbf{r}')}{|\mathbf{r}-\mathbf{r}'|}d\mathbf{r}d\mathbf{r}' = \int\sum_i\psi_i^{s*}(\boldsymbol{r}')\frac{q^2}{|\boldsymbol{r}-\boldsymbol{r}'|}\psi_i^s(\boldsymbol{r}')d\boldsymbol{r}'$$

$$\frac{\partial}{\partial n(\boldsymbol{r})}U_{ext}[n] = \frac{\partial}{\partial n(\boldsymbol{r})}\int\ V_{ext}(\boldsymbol{r})n(\boldsymbol{r})d\boldsymbol{r} = V_{ext}(\boldsymbol{r})$$

$$\frac{\partial}{\partial n(\boldsymbol{r})}E_{xc}[n] = V_{xc}(\boldsymbol{r}) \qquad \text{Just defining the exchange-correlation potential as the derivative of } E_{xc}[n]$$

Now we just need to plug all the derivatives back in the equation:

$$\frac{\partial}{\partial\psi_j^{s*}(\boldsymbol{r})}T_s[n] + \frac{\partial}{\partial n(\boldsymbol{r})}\Big(U_s[n]+U_{ext}[n]+E_{xs}[n]\Big)\psi_j^s(\boldsymbol{r}) = \lambda_j\psi_j^s(\boldsymbol{r}_j)$$

$$\frac{-\hbar^2\nabla_j^2}{2m}\psi_j\int\sum_i\psi_i^{s*}(\boldsymbol{r}')\frac{q^2}{|\boldsymbol{r}-\boldsymbol{r}'|}\psi_i^s(\boldsymbol{r}')d\boldsymbol{r}' + V_{ext}(\boldsymbol{r}) + V_{xc}(\boldsymbol{r})\Big)\psi_j^s(\boldsymbol{r}_j) = \epsilon_j^s\psi_j^s(\boldsymbol{r}_j)$$

$$\Big(\frac{-\hbar^2\nabla_j^2}{2m} + \int\sum_i\psi_i^{s*}(\boldsymbol{r}')\frac{q^2}{|\boldsymbol{r}-\boldsymbol{r}'|}\psi_i^s(\boldsymbol{r}')d\boldsymbol{r}' + V_{ext}(\boldsymbol{r}) + V_{xc}(\boldsymbol{r})\Big)\psi_j^s(\boldsymbol{r}_j) = \epsilon_j^s\psi_j^s(\boldsymbol{r}_j)$$

This is the Kohn-Sham single-electron equation. In practice, for condensed matter one solves this equation in the reciprocal space.

To simplify this expression, we will include the self interaction. This is of course an approximation, but it simplifies the calculations considerably:

$$\Big(\frac{-\hbar^2\nabla_j^2}{2m} + \int \sum_i \psi_i^{s*}(\boldsymbol{r}')\frac{q^2}{|\boldsymbol{r}-\boldsymbol{r}'|}\psi_i^s(\boldsymbol{r}')d\boldsymbol{r}' + V_{ext}(\boldsymbol{r}) + V_{xc}(\boldsymbol{r})\Big)\psi_j^s(\boldsymbol{r}_j) = \epsilon_j^s\psi_j^s(\boldsymbol{r}_j)$$

$$\Big(\frac{-\hbar^2\nabla_j^2}{2m} + \int q^2\frac{n(\boldsymbol{r}')}{|\boldsymbol{r}-\boldsymbol{r}'|}d\boldsymbol{r}' + V_{ext}(\boldsymbol{r}) + V_{xc}(\boldsymbol{r})\Big)\psi_j^s(\boldsymbol{r}_j) = \epsilon_j^s\psi_j^s(\boldsymbol{r}_j)$$

$$\Big(\frac{-\hbar^2\nabla_j^2}{2m} + V_H(\boldsymbol{r}) + V_{ext}(\boldsymbol{r}) + V_{xc}(\boldsymbol{r})\Big)\psi_j^s(\boldsymbol{r}_j) = \epsilon_j^s\psi_j^s(\boldsymbol{r}_j), \quad V_H(\boldsymbol{r}) = \int q^2\frac{n(\boldsymbol{r}')}{|\boldsymbol{r}-\boldsymbol{r}'|}d\boldsymbol{r}'$$

$$\Big(\frac{-\hbar^2\nabla_j^2}{2m} + V_{eff}(\boldsymbol{r})\Big)\psi_j^s(\boldsymbol{r}_j) = \epsilon_j^s\psi_j^s(\boldsymbol{r}_j), \quad V_{eff}(\boldsymbol{r}) = V_H(\boldsymbol{r}) + V_{ext}(\boldsymbol{r}) + V_{xc}(\boldsymbol{r})$$

This is the KS equation (with self-interaction error).

The equation above does not give us the total energy. We need an additional expression for that. Just like for the Hartree equation, we derive an expression for the total energy that does not contain wavefunctions. Thus, we shall eliminate the kinetic energy. This is done by:

$$\int \sum_j \psi_j^{s*}(\boldsymbol{r})d\boldsymbol{r} \times \Big(\frac{-\hbar^2\nabla_j^2}{2m} + V_H(\boldsymbol{r}) + V_{ext}(\boldsymbol{r}) + V_{xc}(\boldsymbol{r})\Big)\psi_j^s(\boldsymbol{r}_j) = \epsilon_j^s\psi_j^s(\boldsymbol{r}_j) \times \int \sum_j \psi_j^{s*}(\boldsymbol{r})d\boldsymbol{r}$$

$$T_s[n] + \int \sum_j \psi_j^{s*}(\boldsymbol{r})d\boldsymbol{r}\Big(\int q^2\frac{n(\boldsymbol{r}')}{|\boldsymbol{r}-\boldsymbol{r}'|}d\boldsymbol{r}' + V_{ext}(\boldsymbol{r}) + V_{xc}(\boldsymbol{r})\Big)\psi_j^s(\boldsymbol{r}_j) = \sum_j \epsilon_j^s$$

$$T_s[n] + \int\int q^2\frac{n(\boldsymbol{r})n(\boldsymbol{r}')}{|\boldsymbol{r}-\boldsymbol{r}'|}d\boldsymbol{r}d\boldsymbol{r}' + \int V_{ext}(\boldsymbol{r})n(\boldsymbol{r})d\boldsymbol{r} + \int V_{xc}(\boldsymbol{r})n(\boldsymbol{r})d\boldsymbol{r} = \sum_j \epsilon_j^s$$

$$T_s[n] + \int\int q^2\frac{n(\boldsymbol{r})n(\boldsymbol{r}')}{|\boldsymbol{r}-\boldsymbol{r}'|}d\boldsymbol{r}d\boldsymbol{r}' + U_{ext}[n] + \int V_{xc}(\boldsymbol{r})n(\boldsymbol{r})d\boldsymbol{r} = \sum_j \epsilon_j^s$$

$$T_s[n] = \sum_j \epsilon_j^s - \int\int q^2\frac{n(\boldsymbol{r})n(\boldsymbol{r}')}{|\boldsymbol{r}-\boldsymbol{r}'|}d\boldsymbol{r}d\boldsymbol{r}' - U_{ext}[n] - \int V_{xc}(\boldsymbol{r})n(\boldsymbol{r})d\boldsymbol{r}$$

Now if we use this definition of $T_s[n]$ and plug it into the total energy, we get:

$$E[n] = T_s[n] + U_s[n] + U_{ext}[n] + E_{xc}[n]$$

$$E[n] = \sum_j \epsilon_j^s - q^2\int\int \frac{n(\boldsymbol{r})n(\boldsymbol{r}')}{|\boldsymbol{r}-\boldsymbol{r}'|}d\boldsymbol{r}d\boldsymbol{r}' - U_{ext}[n] - \int V_{xc}(\boldsymbol{r})n(\boldsymbol{r})d\boldsymbol{r} + U_s[n] + U_{ext}[n] + E_{xc}[n]$$

$$E[n] = \sum_j \epsilon_j^s - \frac{q^2}{2}\int\int \frac{n(\boldsymbol{r})n(\boldsymbol{r}')}{|\boldsymbol{r}-\boldsymbol{r}'|}d\boldsymbol{r}d\boldsymbol{r}' - \int V_{xc}(\boldsymbol{r})n(\boldsymbol{r})d\boldsymbol{r} + E_{xc}[n]$$

There is an important difference between the Hartree approximation and the KS equation: the KS equation includes the correct exchange and correlation energies $E_{xc}[n]$. The Hartree can never become exact (since it using incorrect wavefunction, though correct Hamiltonian), whereas the KS equation is exact if the exchange-correlation energy is exact (although incorrect wavefunction). Therefore, the "only" thing we have to do now is to find exact $E_{xc}[n]$ as functional of the density $n(\boldsymbol{r})$. With such expression, we can derive with respect to density to generate $V_{xc}(\boldsymbol{r}) = \frac{\partial E_{xc}[n]}{\partial n}$. Since we have not the exact expression of $E_{xc}[n]$, we need an approximation to it [17].